

Contribution of Radio Halos to the Foreground for SKA EoR Experiments

WEITIAN LI,¹ HAIGUANG XU,^{1,2,3} ZHIXIAN MA,⁴ DAN HU,¹ ZHENGHUA ZHU,¹ CHENXI SHAN,¹ JINGYING WANG,⁵ JUNHUA GU,⁶ DONGCHAO ZHENG,¹ XIAOLI LIAN,¹ QIAN ZHENG,⁷ YU WANG,⁸ JIE ZHU,⁴ AND XIANG-PING WU⁶

¹*School of Physics and Astronomy, Shanghai Jiao Tong University, 800 Dongchuan Road, Shanghai 200240, China*

²*Tsung-Dao Lee Institute, Shanghai Jiao Tong University, 800 Dongchuan Road, Shanghai 200240, China*

³*IFSA Collaborative Innovation Center, Shanghai Jiao Tong University, 800 Dongchuan Road, Shanghai 200240, China*

⁴*Department of Electronic Engineering, Shanghai Jiao Tong University, 800 Dongchuan Road, Shanghai 200240, China*

⁵*Department of Physics and Astronomy, University of the Western Cape, Cape Town 7535, South Africa*

⁶*National Astronomical Observatories, Chinese Academy of Sciences, 20A Datun Road, Beijing 100012, China*

⁷*Shanghai Astronomical Observatory, Chinese Academy of Sciences, 80 Nandan Road, Shanghai 200030, China*

⁸*School of Mathematics, Physics and Statistics, Shanghai University of Engineering Science, 333 Longteng Road, Shanghai 201620, China*

(Received 2018 August 14; Revised 2019 March 26; Accepted 2019 May 13)

Submitted to ApJ

ABSTRACT

The overwhelming foreground contamination is one of the primary impediments to probing the Epoch of Reionization (EoR) through measuring the redshifted 21 cm signal. Among various foreground components, radio halos are less studied and their impacts on the EoR observations are still poorly understood. In this work, we employ the Press–Schechter formalism, merger-induced turbulent reacceleration model, and the latest SKA1-Low layout configuration to simulate the SKA “observed” images of radio halos. We calculate the one-dimensional power spectra from simulated images and find that radio halos can be about 10^4 , 10^3 , and $10^{2.5}$ times more luminous than the EoR signal on scales of $0.1 \text{ Mpc}^{-1} < k < 2 \text{ Mpc}^{-1}$ in the 120–128, 154–162, and 192–200 MHz bands, respectively. By examining the two-dimensional power spectra inside properly defined EoR windows, we find that the power leaked by radio halos can still be significant, as the power ratios of radio halos to the EoR signal on scales of $0.5 \text{ Mpc}^{-1} \lesssim k \lesssim 1 \text{ Mpc}^{-1}$ can be up to about 230–800%, 18–95%, and 7–40% in the three bands when the 68% uncertainties caused by the variation of the number density of bright radio halos are considered. Furthermore, we find that radio halos located inside the far side lobes of the station beam can also impose strong contamination within the EoR window. In conclusion, we argue that radio halos are severe foreground sources and need serious treatments in future EoR experiments.

Keywords: dark ages, reionization, first stars — early universe — galaxies: clusters: intracluster medium — methods: data analysis — techniques: interferometric

1. INTRODUCTION

The Epoch of Reionization (EoR; $z \sim 6$ –15) refers to a period of our universe preceded by the Cosmic Dawn ($z \sim 15$ –30) and the Dark Ages ($z \sim 30$ –200) and is expected to last from about 300 million to about 1 billion years after the big bang (see Koopmans et al. 2015

and references therein). During the EoR, the reionization of neutral hydrogen (H I), which was caused primarily by the ultraviolet and soft X-ray photons emitted from the first-generation celestial objects, efficiently surpassed the cooling of the gas (Dayal & Ferrara 2018). As a result, the majority of baryonic matter was again in a highly ionized state. Comparing with the observations of distant quasars and cosmic microwave background (CMB), which have provided some important but loose constraints on the reionization process (see Fan et al. 2006 for a review), the 21 cm line emission of H I that

Corresponding author: Haiguang Xu

hgxu@sjtu.edu.cn

liweitianux@sjtu.edu.cn

is redshifted to frequencies below 200 MHz is regarded as the decisive probe to directly explore the EoR (see Furlanetto *et al.* 2006; Zaroubi 2013; Furlanetto 2016, for reviews).

In order to probe the EoR, a number of radio interferometers working at the low-frequency radio bands (\sim 50–200 MHz) have been designed to target the redshifted 21 cm signal, among which there are the Square Kilometre Array (SKA; Mellema *et al.* 2013; Koopmans *et al.* 2015), the Hydrogen Epoch of Reionization Array (HERA; DeBoer *et al.* 2017), and their pathfinders, such as the LOw Frequency ARray (LOFAR; van Haarlem *et al.* 2013), the Murchison Widefield Array (MWA; Bowman *et al.* 2013; Tingay *et al.* 2013), the Precision Array for Probing the Epoch of Reionization (PAPER; Parsons *et al.* 2010), and the 21 CentiMeter Array (21CMA; Zheng *et al.* 2016). The challenges met in these experiments, however, are immense due to a variety of complicated instrumental effects, ionospheric distortions, radio frequency interference, and the strong celestial foreground contamination that overwhelms the redshifted 21 cm signal by about four to five orders of magnitude (see Morales & Wyithe 2010, for a review).

Among various contaminating foreground components, the Galactic diffuse radiation (including both the synchrotron and free-free emissions) and extragalactic point sources are the most prominent and contribute the majority of the foreground contamination (e.g., Shaver *et al.* 1999; Di Matteo *et al.* 2004; Gleser *et al.* 2008; Liu & Tegmark 2012; Murray *et al.* 2017; Spinelli *et al.* 2018). At about 150 MHz, it is estimated that they may account for about 71% and 27% of the total foreground contamination, respectively (Shaver *et al.* 1999). Most of the remaining foreground contamination arises from the emission from the extragalactic diffuse sources that include the large-scale filaments embedded in cosmic webs (e.g., Vazza *et al.* 2015), the intergalactic medium located at cluster outskirts (e.g., Keshet *et al.* 2004), and the intracluster medium (ICM) of galaxy clusters (radio halos, relics, and mini-halos; e.g., Feretti *et al.* 2012). There is only limited observational evidence, especially in the low-frequency regime, of these diffuse sources. Among them, radio halos have gained relatively more observational constraints and theoretical understanding, which enables us to effectively evaluate their contamination on the EoR observations.

First discovered in the Coma cluster (Large *et al.* 1959), radio halos have been observed in about 80 merging galaxy clusters, exhibiting relatively regular morphologies and about Mpc spatial extensions. It should be noted that the angular sizes of radio halos appear to be several to tens of arcminutes, which coincide with

those of the ionizing bubbles during the EoR. This, complemented by the potentially large number (several to tens of thousands in the whole sky) of radio halos to be revealed by the forthcoming low-frequency radio telescopes (e.g., Cassano *et al.* 2015), indicates that radio halos might be important contaminating foreground sources (e.g., Di Matteo *et al.* 2004; Gleser *et al.* 2008). As of today, however, only very few works have been dedicated to this topic and are all based on relatively straightforward modeling methods, such as using the 1.4 GHz radio flux function or radio–X-ray scaling relations that are barely constrained by the very limited observations (e.g., Gleser *et al.* 2008; Jelić *et al.* 2008). In this work, we focus on the radio halos and employ a semi-analytic approach to derive their low-frequency emission maps with the SKA1-Low’s instrumental effects incorporated. By making use of the power spectra and the EoR window, the contamination of radio halos on the EoR observations is quantitatively evaluated for both foreground removal and avoidance methods, which are the two major categories of methods that proposed to tackle the foreground contamination (see Chapman *et al.* 2016 and references therein).

This paper is prepared as follows. In Section 2, we simulate the low-frequency radio sky, where a semi-analytic simulation of radio halos is developed by employing the Press–Schechter formalism and turbulent reacceleration model. In Section 3, we adopt the latest SKA1-Low layout configuration to incorporate the practical instrumental effects into the simulated sky maps. We briefly introduce the power spectra and the EoR window in Section 4 and then quantitatively evaluate the contamination caused by radio halos on the EoR measurements in Section 5. In Section 6, we discuss how the EoR detection is affected by radio halos due to the instrumental frequency artifacts and the far side lobes of the station beam. Finally, we summarize our work in Section 7. Throughout this work we adopt a flat Λ CDM cosmology with $H_0 = 100 h = 71 \text{ km s}^{-1} \text{ Mpc}^{-1}$, $\Omega_m = 0.27$, $\Omega_\Lambda = 1 - \Omega_m = 0.73$, $\Omega_b = 0.046$, $n_s = 0.96$, and $\sigma_8 = 0.81$. The quoted uncertainties are at 68% confidence level unless otherwise stated.

2. SIMULATION OF RADIO SKY

Based on our previous works (Wang *et al.* 2010, 2013), we have developed the FG21sim¹ software to simulate the low-frequency radio sky by taking into account the contributions of our Galaxy, extragalactic point sources, and radio halos in galaxy clusters. We choose three representative frequency bands, namely 120–128,

¹ FG21sim: <https://github.com/liweitianux/fg21sim>

154–162, and 192–200 MHz, and perform simulations for a sky patch of size $10^\circ \times 10^\circ$. The 8 MHz bandwidth is chosen to limit the effect of cosmological evolution of the EoR signal when calculating power spectra (e.g. Wyithe & Loeb 2004; Thyagarajan et al. 2013). The simulated sky maps are pixelized into 1800×1800 with a pixel size of $20''$.

2.1. Radio Halos in Galaxy Clusters

As a significant improvement over our past works (Wang et al. 2010, 2013), we model the radio halos in galaxy clusters by employing the Press–Schechter formalism and turbulent reacceleration model, which was pioneered by Brunetti et al. (2001) and Petrosian (2001) and further developed in many works (e.g., Fujita et al. 2003; Brunetti et al. 2004; Cassano & Brunetti 2005; Brunetti & Lazarian 2007, 2011) to explain the observed properties and formation of radio halos (see Brunetti & Jones 2014 for a recent review). In the framework of reacceleration model, relativistic electrons in the ICM are reaccelerated by the turbulence generated in merger events via the second-order Fermi process, and lose energies due to mechanisms including synchrotron radiation, inverse Compton scattering off the CMB photons, and Coulomb collisions with the thermal ICM. For a galaxy cluster, we first simulate its merging history according to the extended Press–Schechter theory and then derive the temporal evolution of the relativistic electron spectrum by applying the reacceleration model. Finally, the radio halo associated with the galaxy cluster is identified and its synchrotron radiation is determined.

2.1.1. Mass Function

The Press–Schechter formalism was originally advanced as one of the standard methods to predict the mass function of galaxy clusters and their evolution in the universe (Press & Schechter 1974) and has been extended to combine with the cold dark matter (CDM) models (e.g., Bond et al. 1991; Lacey & Cole 1993). In this formalism, the number of galaxy clusters per unit of comoving volume at redshift z in the mass range $[M, M + dM]$ is

$$n(M, z) dM = \sqrt{\frac{2}{\pi}} \frac{\langle \rho \rangle}{M} \frac{\delta_c(z)}{\sigma^2(M)} \left| \frac{d\sigma(M)}{dM} \right| \times \exp \left[-\frac{\delta_c^2(z)}{2\sigma^2(M)} \right] dM, \quad (1)$$

where M is the virial mass of galaxy clusters, $\langle \rho \rangle$ is the current mean density of the universe, $\delta_c(z)$ is the critical linear overdensity for a region to collapse at redshift z [see Equation (A1)], and $\sigma(M)$ is the current root-

mean-square (rms) density fluctuations within a sphere of mean mass M .

Considering the CDM model and the mass range covered by galaxy clusters, it is reasonable to adopt the following power-law distribution for the density perturbations (Randall et al. 2002; Sarazin 2002)

$$\sigma(M) = \sigma_8 \left(\frac{M}{M_8} \right)^{-\alpha}, \quad (2)$$

where σ_8 is the current rms density fluctuation on a scale of $8 h^{-1}$ Mpc, $M_8 = (4\pi/3)(8 h^{-1}$ Mpc) $^3 \langle \rho \rangle$ is the mass contained in a sphere of radius $8 h^{-1}$ Mpc, and the exponent $\alpha = (n+3)/6$ with $n = -7/5$ (Randall et al. 2002) is related to the fluctuation pattern whose power spectrum varies with wave number k as k^n .

With a minimum galaxy cluster mass of $M_{\min} = 2 \times 10^{14} M_\odot$ and a maximum redshift cut at $z_{\max} = 4$, we apply Equation (1) and calculate that the total number of galaxy clusters in a $10^\circ \times 10^\circ$ sky patch is 504. Then the galaxy cluster sample is built by randomly drawing mass and redshift pairs $(M_{\text{sim}}, z_{\text{sim}})$ from the mass and redshift distributions as shown in Figure 1, which are determined by the Press–Schechter mass function [Equation (1)].

2.1.2. Merging History

The extended Press–Schechter theory outlined in Lacey & Cole (1993) provides a way to describe the growth history of galaxy clusters in terms of the merger tree. In order to build the merger tree for a galaxy cluster, we start with its “current” mass M_{sim} and redshift z_{sim} obtained in Section 2.1.1, and trace its growth history back in time by running Monte Carlo simulations to randomly determine the mass change ΔM at each step, which may be regarded either as a merger event (if $\Delta M > \Delta M_c$) or as an accretion event (if $\Delta M \leq \Delta M_c$). Since radio halos are usually associated with major mergers, we choose $\Delta M_c = 10^{13} M_\odot$ (e.g., Cassano & Brunetti 2005).

We assume that, during each growth step, the cluster mass increases from M_1 at time t_1 to M_2 at a later time t_2 ($> t_1$). Given M_2 and t_2 , the conditional probability of the cluster had a progenitor of mass in the range $[M_1, M_1 + dM_1]$ at an earlier time t_1 can be expressed as

$$\Pr(M_1, t_1 | M_2, t_2) dM_1 = \frac{1}{\sqrt{2\pi}} \frac{M_2}{M_1} \frac{\delta_{c1} - \delta_{c2}}{(\sigma_1^2 - \sigma_2^2)^{3/2}} \times \left| \frac{d\sigma_1^2}{dM_1} \right| \exp \left[-\frac{(\delta_{c1} - \delta_{c2})^2}{2(\sigma_1^2 - \sigma_2^2)} \right] dM_1, \quad (3)$$

where $\delta_{ci} \equiv \delta_c(t_i)$, $\sigma_i \equiv \sigma(M_i)$, and $i = 1, 2$ are used to denote parameters defined at time t_1 and t_2 , respectively

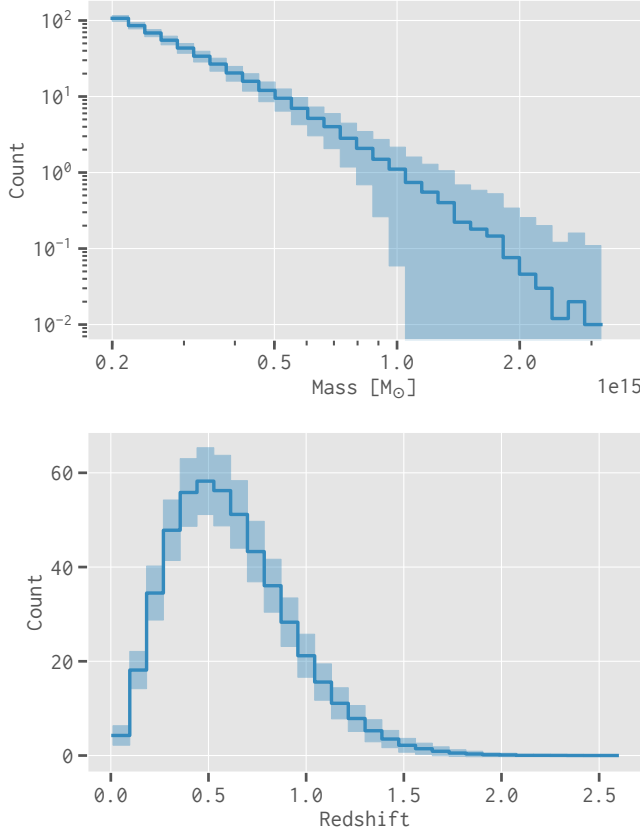


Figure 1. The mass (upper panel) and redshift (lower panel) histograms of the simulated galaxy clusters in a $10^\circ \times 10^\circ$ sky patch. The solid lines and shaded regions represent the means and 68% uncertainties derived from 500 simulation runs, respectively.

(Lacey & Cole 1993; Randall et al. 2002). By further introducing $S \equiv \sigma^2(M)$ and $\omega \equiv \delta_c(t)$, this equation reduces to

$$\Pr(\Delta S, \Delta \omega) d\Delta S = \frac{1}{\sqrt{2\pi}} \frac{\Delta \omega}{(\Delta S)^{3/2}} \exp\left[-\frac{(\Delta \omega)^2}{2\Delta S}\right] d\Delta S. \quad (4)$$

In order to resolve mergers with a mass change $\Delta M_c \ll M$ during the backward tracing of a galaxy cluster, a time step Δt (i.e., $\Delta \omega$) that satisfies

$$\Delta \omega \lesssim \Delta \omega_{\max} = \left[S \left| \frac{d \ln \sigma^2}{d \ln M} \right| \left(\frac{\Delta M_c}{M} \right) \right]^{1/2} \quad (5)$$

is required (Lacey & Cole 1993), and we adopt an adaptive step of $\Delta \omega = \Delta \omega_{\max}/2$ (Randall et al. 2002). At a certain step when $\Delta \omega$ is given, the mass change ΔS can be randomly drawn from the following cumulative

probability distribution of subcluster masses

$$\Pr(<\Delta S, \Delta \omega) = \int_0^{\Delta S} \Pr(\Delta S', \Delta \omega) d\Delta S' \quad (6)$$

$$= 1 - \text{erf}\left(\frac{\Delta \omega}{\sqrt{2\Delta S}}\right), \quad (7)$$

where $\text{erf}(x) = (2/\sqrt{\pi}) \int_0^x e^{-t^2} dt$ is the error function. Then, the cluster's progenitor mass M_1 is obtained as $S_1 = S_2 + \Delta S$.

Given that observable radio halos are regarded to be associated with recent (in the observer's frame) major mergers and have typical lifetimes of $\tau_{\text{halo}} \lesssim 1$ Gyr at 1.4 GHz (e.g., Brunetti et al. 2009; Cassano et al. 2016), we trace the merging history of each galaxy cluster for $t_{\text{back}} = 3$ Gyr from its “current” age t_{sim} (corresponding to z_{sim}). For each built merger tree, we extract the information of all the mergers associated with the main cluster to carry out the subsequent simulation of radio halos. As shown in the upper panel of Figure 2, we took one galaxy cluster of mass $10^{15} M_{\odot}$ as an example and repeated the random merger tree build process for 30 times. We also randomly drew 30 galaxy clusters from the sample constructed in Section 2.1.1 and built one merger tree instance for each galaxy cluster, as shown in the lower panel.

2.1.3. Evolution Modeling

According to the reacceleration model, there exists a population of primary (or fossil) high-energy electrons, which permeate the ICM and are thought to be injected by multiple processes, such as active galactic nucleus (AGN) activities and star formations (see Blasi et al. 2007 for a review). When a cluster experiences a major merger, the turbulence is generated throughout the ICM and can accelerate the primary electrons to be highly relativistic, resulting in the observed radio halo. On the other hand, relativistic electrons in the ICM lose energy via mechanisms that include synchrotron radiation, inverse Compton scattering off the CMB photons, and Coulomb collisions (Sarazin 1999). For a population of electrons with isotropic energy distribution, the temporal evolution of the number density distribution $n(\gamma, t)$ is governed by the following Fokker–Planck diffusion–advection equation (Eilek & Hughes 1991; Schlickeiser 2002)

$$\begin{aligned} \frac{\partial n(\gamma, t)}{\partial t} = & \frac{\partial}{\partial \gamma} \left[n(\gamma, t) \left(\left| \frac{d\gamma}{dt} \right| - \frac{2}{\gamma} D_{\gamma\gamma}(\gamma, t) \right) \right] \\ & + \frac{\partial}{\partial \gamma} \left[D_{\gamma\gamma} \frac{\partial n(\gamma, t)}{\partial \gamma} \right] + Q_e(\gamma, t), \end{aligned} \quad (8)$$

where γ is the Lorentz factor of electrons, $D_{\gamma\gamma}(\gamma, t)$ is the diffusion coefficient describing the interactions

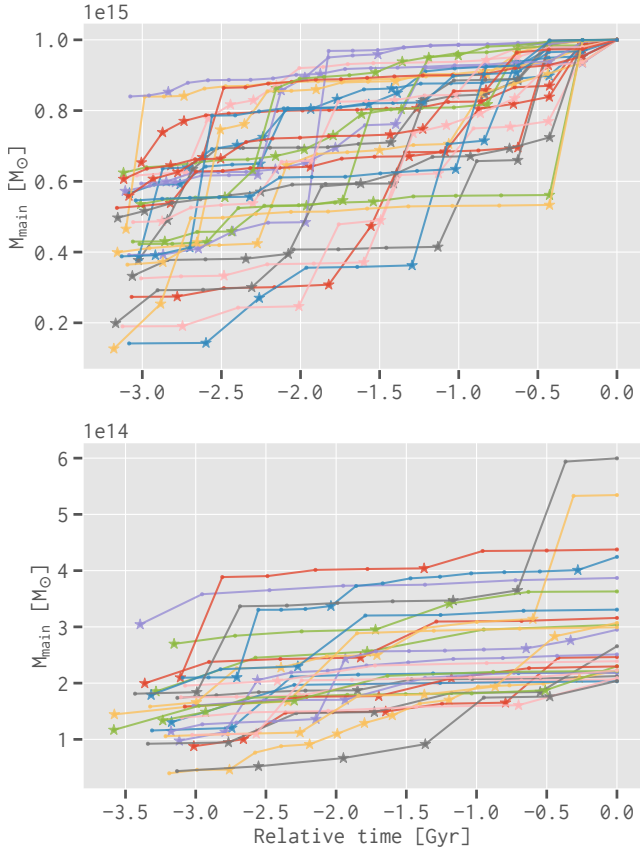


Figure 2. (**Upper**) Merger trees for one galaxy cluster of mass $10^{15} M_{\odot}$ obtained by repeating the random build process for 30 times. (**Lower**) Example merger trees for 30 galaxy clusters randomly drawn from the sample constructed in Section 2.1.1. Asterisks mark merger events and dots represent accretion events.

between the turbulence and electrons, $|d\gamma/dt|$ is the energy-loss rate, and $Q_e(\gamma, t)$ describes the electron injection.

a. Thermal Properties of the ICM

The number density of thermal electrons n_{th} in the ICM can be calculated as

$$n_{\text{th}} \simeq \frac{3f_{\text{gas}}M_{\text{vir}}}{4\pi\mu m_u r_{\text{vir}}^3}, \quad (9)$$

where $\mu \simeq 0.6$ is the mean molecular weight (e.g., Ettori et al. 2013), m_u is the atomic mass unit, M_{vir} is the cluster's virial mass, r_{vir} is the virial radius [see Equation (A5)], and $f_{\text{gas}} \simeq \Omega_b/\Omega_m$ is the assumed gas mass fraction. Then, the corresponding ICM thermal energy density ϵ_{th} is given by

$$\epsilon_{\text{th}} = \frac{3}{2} n_{\text{th}} k_B T_{\text{cl}}. \quad (10)$$

The ICM mean temperature T_{cl} is approximately given by

$$T_{\text{cl}} \simeq T_{\text{vir}} + \frac{3}{2} T_{\text{out}} \quad (11)$$

(Cavaliere et al. 1998), where $T_{\text{vir}} = \mu m_u G M_{\text{vir}} / (2 r_{\text{vir}})$ is the virial temperature and $T_{\text{out}} \simeq 0.5 \text{ keV}$ is the temperature of the gas flowing into the cluster from its outskirts (Fujita et al. 2003).

b. Electron Injection

As primary electrons are continuously injected into the ICM via multiple processes, it is reasonable to assume an average injection rate and a power-law spectrum for the electron injection process (e.g., Cassano & Brunetti 2005; Donnert & Brunetti 2014), i.e.,

$$Q_e(\gamma, t) \simeq Q_e(\gamma) = K_e \gamma^{-s}, \quad (12)$$

where the spectral index s is adopted to be 2.5 (Cassano & Brunetti 2005). Moreover, the energy density of the injected electrons can be assumed to account for a fraction (η_e) of the ICM thermal energy density (Cassano & Brunetti 2005), i.e.,

$$\tau_{\text{cl}} \int_{\gamma_{\min}}^{\gamma_{\max}} Q_e(\gamma') \gamma' \epsilon_e d\gamma' = \eta_e \epsilon_{\text{th}}, \quad (13)$$

where $\tau_{\text{cl}} \simeq t_{\text{sim}}$ is the cluster's age at its “current” redshift z_{sim} , and $\epsilon_e = m_e c^2$ is the electron's rest energy. Given $\gamma_{\min} \ll \gamma_{\max}$, the injection rate K_e is derived to be

$$K_e \simeq \frac{(s-2) \eta_e \epsilon_{\text{th}}}{\epsilon_e \tau_{\text{cl}}} \gamma_{\min}^{s-2}. \quad (14)$$

c. Stripping Radius

When a subcluster merges into the main cluster, the gas at its outer regions is stripped due to the ram pressure (Gunn & Gott 1972). The stripping radius r_s of the subcluster, outside which the stripping is efficient, can be obtained from the equipartition between the ram pressure and the hydrostatic pressure (Cassano & Brunetti 2005), i.e.,

$$\bar{\rho}_m v_{\text{imp}}^2 = \frac{\rho_s(r_s)}{\mu m_u} k_B T_{\text{cl,s}}, \quad (15)$$

where $\bar{\rho}_m = \mu m_u n_{\text{th,m}}$ is the mean gas density of the main cluster, v_{imp} is the impact velocity of the two merging clusters, and $\rho_s(r)$ and $T_{\text{cl,s}}$ are the gas density profile and temperature of the subcluster, respectively.

Starting from a sufficiently large distance with zero velocity, the impact velocity v_{imp} of two merging clusters with masses $M_{\text{vir,m}}$ and $M_{\text{vir,s}}$ is given by

$$v_{\text{imp}} \simeq \left[\frac{2G(M_{\text{vir,m}} + M_{\text{vir,s}})}{r_{\text{vir,m}}} \left(1 - \frac{1}{\eta_v} \right) \right]^{1/2}, \quad (16)$$

where $\eta_v \simeq 4(1 + M_{\text{vir,s}}/M_{\text{vir,m}})^{1/3}$ (Sarazin 2002; Cassano & Brunetti 2005).

The gas density profile $\rho_s(r)$ can be well approximated with a standard β -model (Cavaliere & Fusco-Femiano 1976):

$$\rho_s(r) = \rho_s(0) [1 + (r/r_{c,s})^2]^{-3\beta/2}, \quad (17)$$

where $r_{c,s}$ and β are the core radius and slope parameter, respectively, and we adopt $r_{c,s} = 0.1 r_{\text{vir,s}}$ (e.g., Sanderson & Ponman 2003) and $\beta = 2/3$ (e.g., Jones & Forman 1984). The central gas density $\rho_s(0)$ can then be determined by the total gas mass ($M_{\text{gas,s}} = f_{\text{gas}} M_{\text{vir,s}}$).

d. Turbulent Acceleration

The details of interactions between the turbulence and both thermal and relativistic particles are complicated and still poorly understood. Among several particle acceleration mechanisms that can be potentially triggered by the turbulence, the most important one is the transit time damping process, i.e., the turbulence dissipates its energy and accelerates particles by interacting with the relativistic particles (e.g., cosmic rays) in the ICM (Brunetti & Lazarian 2007, 2011, and references therein). The associated diffusion coefficient is derived to be (Miniati 2015; Pinzke et al. 2017)

$$D_{\gamma\gamma} = 2\gamma^2 \zeta k_L \frac{\langle(\delta v_t)^2\rangle^2}{\chi_{\text{cr}} c_s^3}, \quad (18)$$

where ζ is an efficiency factor characterizing the ICM plasma instabilities (e.g., due to spatial or temporal intermittency), $\chi_{\text{cr}} = \epsilon_{\text{cr}}/\epsilon_{\text{th}}$ is the relative energy density of cosmic rays with respect to the thermal ICM, $k_L \simeq 2\pi/r_{\text{turb}}$ is the turbulence injection scale with r_{turb} being the radius of the turbulence region, $\langle(\delta v_t)^2\rangle$ is the turbulence velocity dispersion, and c_s is the sound speed in the ICM

$$c_s = \sqrt{\gamma_{\text{gas}} k_B T_{\text{cl}} / (\mu m_u)} \quad (19)$$

with $\gamma_{\text{gas}} = 5/3$ being the adiabatic index of ideal monatomic gas.

In addition to mergers, mechanisms such as outflows from AGNs and galactic winds can introduce turbulence in the ICM, which is found to account for $\lesssim 5\%$ of the thermal energy in the central regions of relaxed clusters (e.g., Vazza et al. 2011). Therefore, the base velocity dispersion $\langle(\delta v_0)^2\rangle$ of the turbulence in the absence of mergers is

$$\langle(\delta v_0)^2\rangle = 3\chi_{\text{turb}} \frac{k_B T_{\text{cl,m}}}{\mu m_u}, \quad (20)$$

where χ_{turb} is the ratio of energy density between the base turbulence and the thermal ICM. A merger will

contribute a significant part of its energy to the turbulence and greatly increase the turbulence velocity dispersion $\langle(\delta v_t)^2\rangle$, which leads to

$$E_{\text{turb}} = \frac{1}{2} M_{\text{turb}} \langle(\delta v_t)^2\rangle = \frac{1}{2} M_{\text{turb}} \langle(\delta v_0)^2\rangle + \eta_t E_m, \quad (21)$$

where E_m is the energy injected by the subcluster during the merger, η_t is the fraction of injected energy (E_m) transferred into turbulent waves, and M_{turb} is the gas mass enclosed in the turbulence region of radius r_{turb} , i.e.,

$$M_{\text{turb}} = \int_0^{r_{\text{turb}}} \rho(r) 4\pi r^2 dr, \quad (22)$$

where $\rho(r)$ is the gas density profile of the merged cluster characterized by the β -model [see Equation (17)]. The injected energy E_m is approximated as the work done by the infalling subcluster, i.e.,

$$E_m \simeq \bar{\rho}_m v_{\text{imp}}^2 V_{\text{turb}}, \quad (23)$$

with $V_{\text{turb}} \simeq \pi r_s^2 r_{\text{vir,m}}$ being the swept volume (Fujita et al. 2003; Cassano & Brunetti 2005). Therefore, the turbulence velocity dispersion during a merger is obtained as

$$\langle(\delta v_t)^2\rangle = \langle(\delta v_0)^2\rangle + 2\pi \eta_t \bar{\rho}_m r_{\text{vir,m}} \frac{r_s^2 v_{\text{imp}}^2}{M_{\text{turb}}}. \quad (24)$$

One remaining parameter is the turbulence region radius r_{turb} , which is estimated to be

$$r_{\text{turb}} = r_s + r_{\text{c,m}}, \quad (25)$$

where $r_{\text{c,m}} = 0.1 r_{\text{vir,m}}$ is the core radius of the main cluster, and r_s is the stripping radius of the subcluster [see Equation (15)] with a value of $\sim 1\text{--}2 r_{\text{c,m}}$ for major mergers ($M_{\text{vir,m}}/M_{\text{vir,s}} \lesssim 3$) and $< r_{\text{c,m}}$ for minor mergers ($M_{\text{vir,m}}/M_{\text{vir,s}} \sim 3\text{--}10$). This assumption is well consistent with previous simulation studies, which show that mergers introduce turbulence in regions of radius about $0.1\text{--}0.3 r_{\text{vir,m}}$ (e.g., Vazza et al. 2011, 2012; Miniati & Beresnyak 2015). We note that minor mergers can also generate a relatively large turbulence region of radius about $r_{\text{c,m}}$ due to the core gas sloshing induced by the infalling subcluster (Vazza et al. 2012). However, the generated turbulence by a minor merger is rather weak because the injected energy E_m is much less than a major one [see Equation (23)].

e. Energy Losses

Among the mechanisms through which relativistic electrons in the ICM can lose energy, we take into account the following three major mechanisms in this work (Sarazin 1999). The first one is the inverse Compton

scattering off the CMB photons, the energy-loss rate of which is

$$\left(\frac{d\gamma}{dt}\right)_{\text{IC}} = -4.32 \times 10^{-4} \gamma^2 (1+z)^4 \quad [\text{Gyr}^{-1}]. \quad (26)$$

Secondly, with the μG -level magnetic field permeating the ICM (e.g., Govoni & Feretti 2004; Ryu et al. 2008), relativistic electrons will produce synchrotron radiation and lose energy at a rate of

$$\left(\frac{d\gamma}{dt}\right)_{\text{syn}} = -4.10 \times 10^{-5} \gamma^2 \left(\frac{B}{1 \mu\text{G}}\right)^2 \quad [\text{Gyr}^{-1}], \quad (27)$$

where B is the magnetic field strength. We assume that the magnetic field is uniform and its energy density reaches equipartition with that of cosmic rays, i.e., $\epsilon_B = B^2/(8\pi) \simeq \epsilon_{\text{cr}} = \chi_{\text{cr}} \epsilon_{\text{th}}$ (Beck & Krause 2005).

The last mechanism considered is that relativistic electrons interact with the thermal electrons via Coulomb collisions, the energy-loss rate of which is

$$\begin{aligned} \left(\frac{d\gamma}{dt}\right)_{\text{Coul}} &= -3.79 \times 10^4 \left(\frac{n_{\text{th}}}{1 \text{ cm}^{-3}}\right) \\ &\times \left[1 + \frac{1}{75} \ln\left(\gamma \frac{1 \text{ cm}^{-3}}{n_{\text{th}}}\right)\right] \quad [\text{Gyr}^{-1}]. \end{aligned} \quad (28)$$

The inverse Compton scattering and synchrotron radiation dominate the energy losses at the high-energy regime ($\gamma \gtrsim 1000$), while Coulomb collisions are the main energy-loss mechanism for electrons with lower energies ($\gamma \lesssim 100$). Therefore, electrons with intermediate energies (e.g., $\gamma \sim 300$) have a long lifetime ($\sim 3 \text{ Gyr}$) and can accumulate in the ICM as the cluster grows (Sarazin 1999).

2.1.4. Numerical Implementation

In order to solve the Fokker–Planck equation [Equation (8)], we apply an efficient numerical method proposed by Chang & Cooper (1970) and adopt the no-flux boundary condition (Park & Petrosian 1996). To avoid the unphysical pile up of electrons around the lower boundary caused by the boundary condition, we define a buffer region below γ_{buf} , within which the spectral data are replaced by extrapolating the data above γ_{buf} as a power-law spectrum (Donnert & Brunetti 2014). We adopt a logarithmic grid with 256 cells for $\gamma \in [1, 10^6]$, and let the buffer region span 10 cells.

By making use of the same Fokker–Planck equation but with the merger-induced turbulent acceleration turned off [i.e., $E_m \equiv 0$ and $\langle (\delta v_t)^2 \rangle \equiv \langle (\delta v_0)^2 \rangle$ in Equation (21)], the initial electron spectrum $n_e(\gamma, t_0)$ is derived by evolving the accumulated electron spectrum $\tilde{n}_e(\gamma) = Q_e(\gamma) \tau_0$ for 1 Gyr (e.g., Brunetti & Lazarian

2007), where τ_0 is the cluster's age at the beginning of the earliest merger.

Although the whole process of a single merger can last for about 2–3 Gyr (e.g., Tormen et al. 2004; Cassano et al. 2016), the period during which the turbulence is intense enough to effectively accelerate electrons is relatively short. An appropriate estimation of the turbulent acceleration period is $\tau_{\text{turb}} \simeq 2 r_{\text{turb}} / v_{\text{imp}}$ (Miniati 2015).

A galaxy cluster may experience multiple mergers in the past $t_{\text{back}} = 3 \text{ Gyr}$. For each merger event $(M_{\text{vir,m}}^{(i)}, M_{\text{vir,s}}^{(i)}, t_{\text{begin}}^{(i)})$, where $t_{\text{begin}}^{(i)}$ denotes the beginning time of this merger, it can induce effective turbulent acceleration (i.e., being active) during the period $[t_{\text{begin}}^{(i)}, t_{\text{end}}^{(i)}]$ with $t_{\text{end}}^{(i)} = t_{\text{begin}}^{(i)} + \tau_{\text{turb}}^{(i)}$ being the time when this merger becomes inactive. At other times (i.e., no active merger), only the base turbulence contributes to the acceleration of electrons, which, however, is insufficient to balance the energy loss due to synchrotron radiation and inverse Compton scattering.

Over the history of a galaxy cluster that has multiple mergers, the turbulence region has a different radius during different mergers. To take this variation into account, we identify the radius of the largest turbulence region (R_{turb}) and properly diffuse the electron spectrum to the sphere of radius R_{turb} for mergers with a smaller turbulence region. Specifically, for a merger that is active during $[t_{\text{begin}}^{(i)}, t_{\text{end}}^{(i)}]$ and has a turbulence region of radius $r_{\text{turb}}^{(i)}$, the accelerated part of the electron spectrum during this merger [i.e., the difference between spectra at $t_{\text{end}}^{(i)}$ and at $t_{\text{begin}}^{(i)}$] is rescaled by a volume ratio given by

$$R_{\text{vol}} = \left[r_{\text{turb}}^{(i)} / R_{\text{turb}}\right]^3. \quad (29)$$

Once the desired electron spectrum $n_e(\gamma, t)$ is obtained, the synchrotron emissivity at a frequency ν is given by

$$J(\nu) = \frac{\sqrt{3} e^3 B}{m_e c^2} \int_{\gamma_{\min}}^{\gamma_{\max}} \int_0^{\pi/2} n_e(\gamma, t) F(\nu/\nu_c) \sin^2 \theta d\theta d\gamma \quad (30)$$

(Rybicki & Lightman 1979), where c is the speed of light, e is the elementary charge, θ is the pitch angle of electrons with respect to the magnetic field, $\nu_c = (3/2) \gamma^2 \nu_L \sin \theta$ is the electron's critical frequency with $\nu_L = eB/(2\pi m_e c)$ being the Larmor frequency, and $F(\cdot)$ is the synchrotron kernel:

$$F(x) = x \int_x^\infty K_{5/3}(y) dy, \quad (31)$$

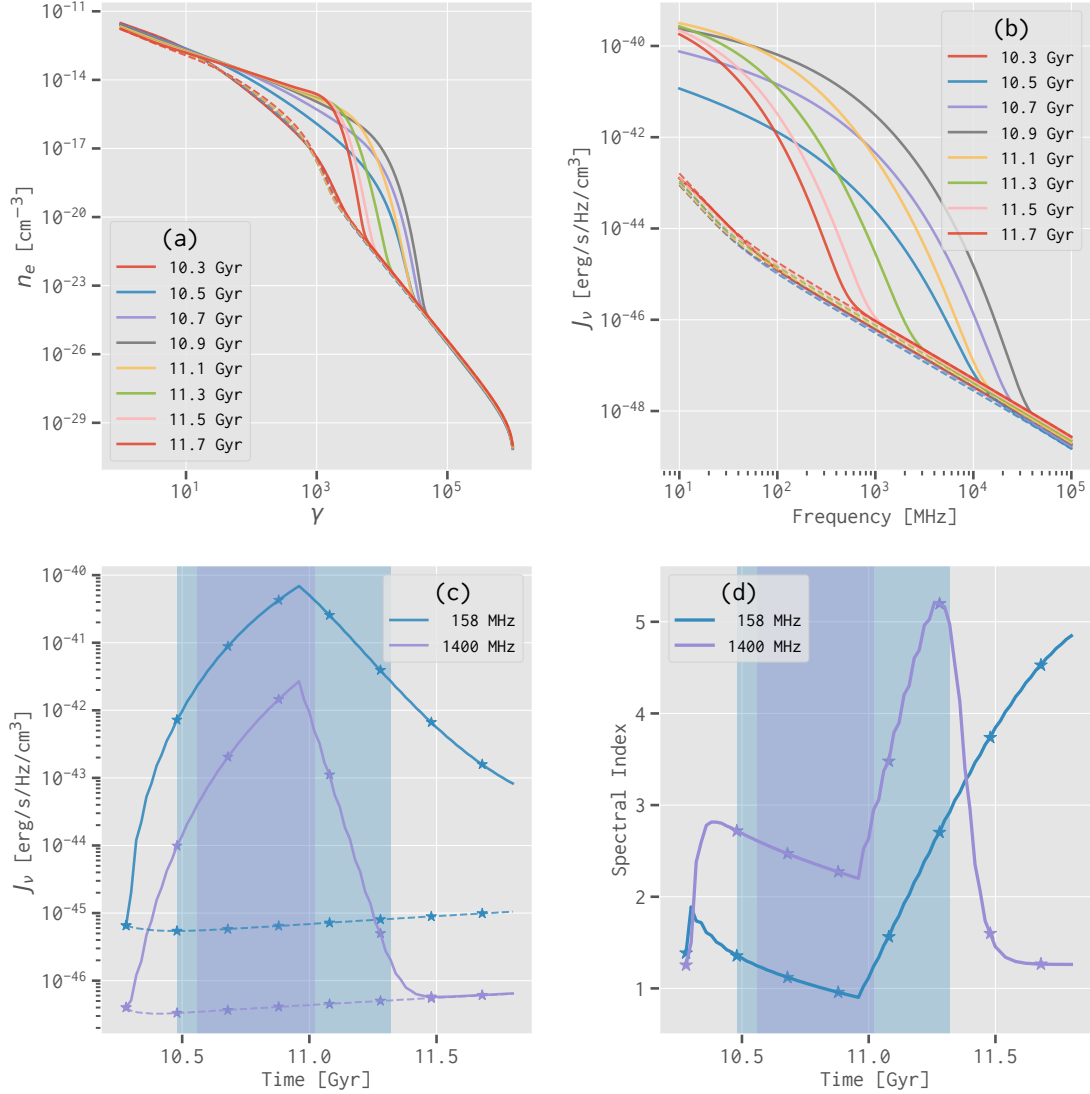


Figure 3. The temporal evolution of the electron and synchrotron emission spectra for an example cluster with one major merger, which begins at redshift $z = 0.3$ (i.e., $t \simeq 10.3$ Gyr) and is tracked until $z = 0.15$ (i.e., $t \simeq 11.8$ Gyr). **(a)** The relativistic electron spectra (solid lines) and the corresponding reference electron spectra (dashed lines; see Section 2.1.5). **(b)** The synchrotron emission spectra (solid lines) and the corresponding reference synchrotron spectra (dashed lines). **(c)** The variation of 158 MHz (solid blue line) and 1400 MHz (solid purple line) synchrotron emissivity as well as the corresponding reference emissivity (dashed lines) with time. **(d)** The temporal variation of spectral indices at 158 MHz (blue line) and 1400 MHz (purple line). Shaded regions show the periods during which the radio halo exists (see Section 2.1.5). Asterisks mark the time points corresponding to the spectra presented in panels (a) and (b).

where $K_{5/3}(\cdot)$ is the modified Bessel function of order 5/3.

In Figure 3, we present the temporal evolution of the relativistic electron and synchrotron emission spectra for an example galaxy cluster with one major merger. The cluster has a mass of $10^{15} M_\odot$ and merges with a subcluster of mass $6 \times 10^{14} M_\odot$ at redshift $z = 0.3$ (i.e., $t \simeq 10.3$ Gyr), from which we solve the Fokker–Planck equation to track the electron and synchrotron emission spectra until redshift $z = 0.15$ (i.e., $t \simeq 11.8$ Gyr). As demonstrated in this figure, the merger-induced turbu-

lence is active for a period of $\tau_{\text{turb}} \simeq 0.67$ Gyr and efficiently accelerates electrons to extremely high energies ($\gamma \gtrsim 10^4$), which gives rise to the radio halo even at high frequencies (> GHz). However, once the turbulence becomes inactive ($t > 10.9$ Gyr), the high-energy electrons quickly lose energy and the radio halo fades out shortly, especially at high frequencies.

2.1.5. Halo Identification and Size

Radio halos cannot form or will rapidly disappear if there is no active turbulent acceleration. In order

to determine whether or not there exists a radio halo at frequency ν , we employ the following two criteria: (1) the synchrotron emissivity $J(\nu)$ of the final electron spectrum $n_e(\gamma, t_{\text{sim}})$ is at least 1000 times larger than the emissivity $J'(\nu)$ of the reference electron spectrum $n'_e(\gamma, t_{\text{sim}})$, which is obtained by solving the identical Fokker–Planck equation but without merger-induced turbulent acceleration, similar to the way of deriving the initial electron spectrum (Section 2.1.4); (2) the spectral index² at frequency ν satisfies $\alpha_\nu \leq 3$. For the example as shown in Figure 3(c,d), a radio halo is identified from about 10.6 to 11.0 Gyr at 1.4 GHz and from about 10.5 to 11.3 Gyr at 158 MHz. The spectral indices at 1.4 GHz and 158 MHz reach about 2.1 and 1.0, respectively. These results demonstrate that radio halos have longer lifetimes at low frequencies and thus we expect to observe more radio halos in low-frequency radio bands. We note that the 1.4 GHz spectral index ($\alpha_{1400} \sim 2.1$) is slightly larger than the general result from observations, because we calculate the spectral index around a specific frequency while observed spectral indices are generally obtained from two separated frequencies (e.g., 0.3 and 1.4 GHz; Feretti et al. 2012).

Previous studies (e.g., Cassano et al. 2007; Basu 2012) have shown that the radius of radio halos (r_{halo}) increases nonlinearly with the cluster's virial radius (r_{vir}), which may be caused by the distributions of relativistic electrons and magnetic fields (e.g., Dolag et al. 2002). Therefore, we assume the following scaling relation for r_{halo} :

$$r_{\text{halo}} = f_r R_{\text{turb}} \left(\frac{r_{\text{vir}}}{r_{\text{vir},*}} \right)^b, \quad (32)$$

where R_{turb} is the radius of the largest turbulence region as also used in Equation (29), $r_{\text{vir},*}$ is the virial radius of a reference cluster of mass $10^{15} M_\odot$, and f_r and b are the scaling normalization and slope, respectively. After comparing with the observed scaling relation of $r_{\text{halo}} \propto r_{\text{vir}}^{2.63 \pm 0.50}$ (Cassano et al. 2007), we obtain $f_r = 0.7$ and $b = 1.8$.

Then, the power of a radio halo at frequency ν is

$$P(\nu) = \frac{4\pi}{3} r_{\text{halo}}^3 J(\nu), \quad (33)$$

and the flux density at the same frequency is

$$S(\nu) = \frac{(1 + z_{\text{sim}}) P(\nu(1 + z_{\text{sim}}))}{4\pi D_L^2(z_{\text{sim}})}, \quad (34)$$

where $D_L(z_{\text{sim}})$ is the luminosity distance to the halo, and the factor $(1 + z_{\text{sim}})$ accounts for the K correction (e.g., Hogg 1999).

² We adopt a power-law spectrum of form $J(\nu) \propto \nu^{-\alpha}$.

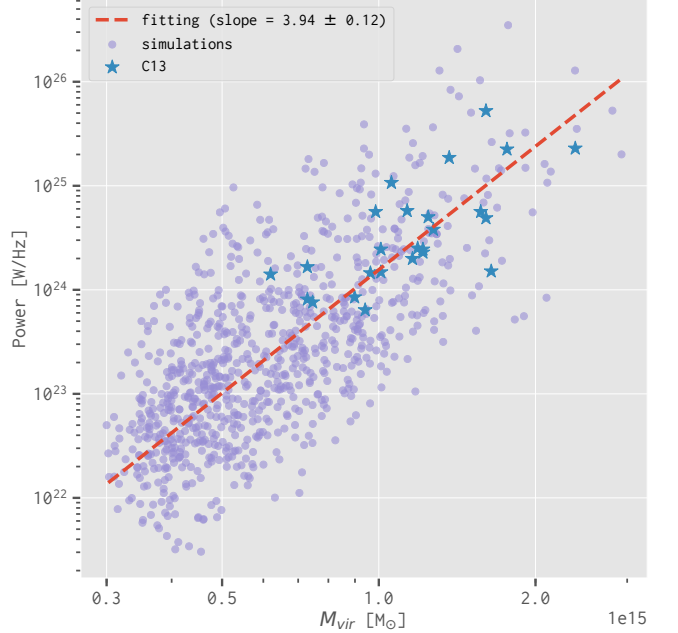


Figure 4. Simulated scaling relation between the radio halo power at 1.4 GHz (P_{1400}) and the cluster mass (M_{vir}). Blue asterisks mark the observation data from Cassano et al. (2013). Purple dots represent the results of 500 simulation runs and the dashed red line shows the fitted relation of $P_{1400} \propto M_{\text{vir}}^{3.94 \pm 0.12}$.

2.1.6. Model Parameters and Results

Our model has the following parameters: (1) η_e , the ratio of the energy density of injected electrons to the thermal energy density; (2) η_t , the fraction of the merger energy transferred into the turbulence; (3) χ_{cr} , the relative energy density of cosmic rays to the thermal component; (4) χ_{turb} , the relative energy density of the base turbulence; (5) ζ , the efficiency of the ICM plasma instabilities. Since currently no reasonable constraints on these parameters can be obtained from either observational or theoretical studies, it is necessary to tune them to make the model predictions (e.g., the halo flux function, the scaling relation between the halo power and the hosting cluster mass) consistent with observations.

We perform two comparisons between our simulations and observations. The first comparison involves the observed scaling relation between the radio halo power at 1.4 GHz (P_{1400}) and the cluster mass (M_{vir}). We make use of the observation data presented by Cassano et al. (2013), who reported a scaling relation of $P_{1400} \propto M_{500}^{3.70 \pm 0.56}$. We convert their mass M_{500} to virial mass by assuming an NFW density profile (Navarro et al. 1997) and employing the mass-concentration relation derived by Duffy et al. (2008). Second, we compare the 1.4 GHz all-sky integrated flux function between the simulated radio halos and obser-

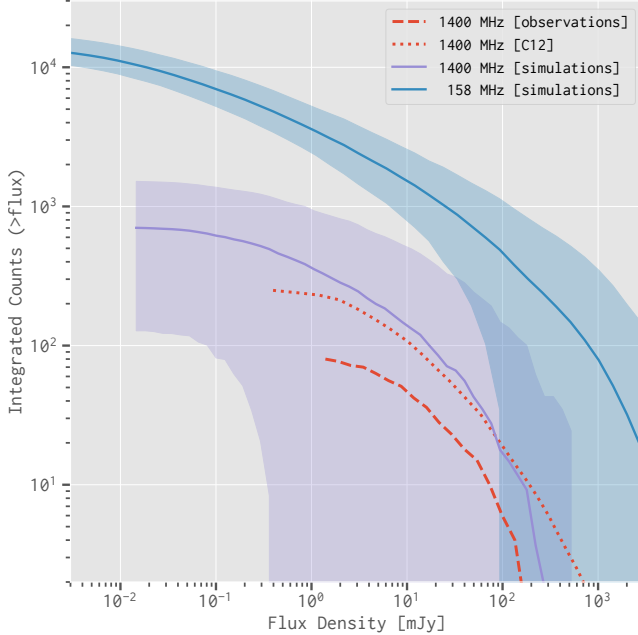


Figure 5. The 1.4 GHz all-sky integrated flux function comparison between the observed (dashed red line) and simulated (solid purple line) radio halos. The dotted red line shows the 1.4 GHz flux function predicted by Cassano et al. (2012). The solid blue line represents the 158 MHz flux function for the simulated halos as a comparison. Shaded regions mark the 68% uncertainties of the simulated radio halos estimated from the 500 simulation runs.

vations. To this end, we have collected all currently observed radio halos (Table B1 in Appendix B; 71 identified halos and 9 candidates; as of 2018 January). Considering that current observations are far from complete, especially at the low-flux end, our strategy is to require that the flux function of simulated radio halos agrees with the observed one at the high-flux end.

We have explored various parameter configurations and, for each configuration, we have repeated the simulation for 500 times in order to take into account the distribution variations of bright radio halos across the sky. By comparing the simulation results with the observed $P_{1400} - M_{\text{vir}}$ scaling relation and the 1.4 GHz flux function, we finally choose a set of model parameters with $\eta_e = 0.01\%$, $\eta_t = 15\%$, $\chi_{\text{cr}} = 1.5\%$, $\chi_{\text{turb}} = 1.5\%$, and $\zeta = 0.1$. As shown in Figure 4, the radio halos simulated by our model with the tuned parameters show a scaling relation of $P_{1400} \propto M_{\text{vir}}^{3.94 \pm 0.12}$, which is consistent with the findings of Cassano et al. (2013) on both the slope and normalization. In Figure 5, we present the 1.4 GHz flux functions for the simulated radio halos and the observed halos, which agree with each other at the high-flux end. The 1.4 GHz flux function given by

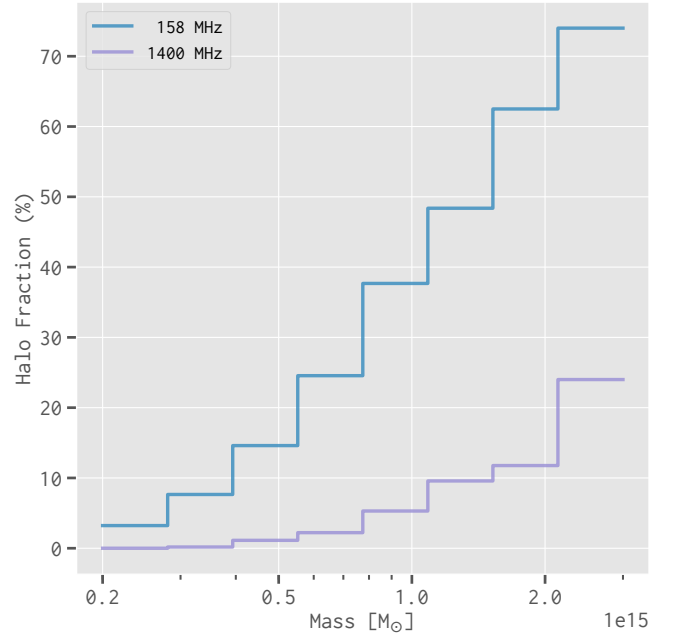


Figure 6. The fraction of clusters with radio halos as a function of the cluster mass. The blue and purple lines represent the fraction of halos identified at 158 MHz and 1.4 GHz, respectively.

our tuned model also matches the prediction of Cassano et al. (2012).

Furthermore, we display the fraction of clusters with radio halos as a function of the cluster mass in Figure 6. It clearly shows that more massive clusters tend to have higher probabilities of hosting radio halos. Meanwhile, we expect to observe many more radio halos at low frequencies (e.g., ~ 100 – 200 MHz), which could be generated by less intense mergers and have longer lifetimes (see also Section 2.1.4 and Figure 3).

2.1.7. Sky Map Generation

To generate images for the simulated radio halos, we adopt an exponential profile for the azimuthally averaged brightness distribution (Murgia et al. 2009):

$$I_\nu(\theta) = I_{\nu,0} \exp(-3\theta/\theta_{\text{halo}}), \quad (35)$$

where $\theta = r/D_A(z_{\text{sim}})$ is the angular radius from the halo center with $D_A(z_{\text{sim}})$ being the angular diameter distance to the halo and $I_{\nu,0} = 9S(\nu)/(2\pi\theta_{\text{halo}}^2)$ is the central brightness.

In order to characterize the uncertainty of the number density of bright radio halos across the sky, we repeat the simulation of radio halos for 100 times. The

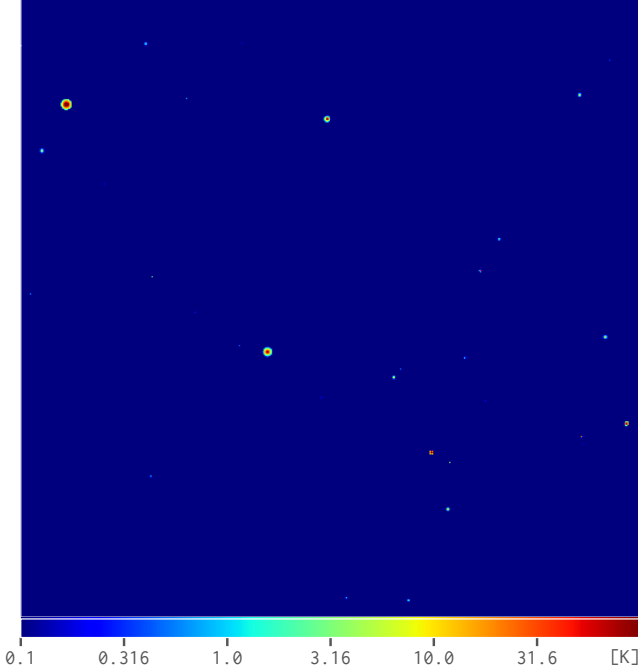


Figure 7. An example from the 100 simulation runs showing the simulated radio halos at 158 MHz. The sky region size is $10^\circ \times 10^\circ$, and the color bar is in units of K.

medians and the corresponding 68% uncertainties³ of the rms brightness temperature are $(4.21^{+11.2}_{-2.60}) \times 10^3$ mK, $(1.81^{+5.28}_{-1.13}) \times 10^3$ mK, and $(0.85^{+2.74}_{-0.54}) \times 10^3$ mK at 124, 158, and 196 MHz, respectively (Table 1; see also Figure 7 for an example map of the simulated radio halos at 158 MHz).

2.2. Other Foreground Components

Following our previous work (Wang et al. 2010), we have also simulated several other foreground components, including the Galactic synchrotron and free-free emissions as well as the extragalactic point sources, in order to carry out comparisons of power spectra between radio halos and other foreground components as an effort to better characterize the contribution of radio halos to the low-frequency radio sky.

The Galactic synchrotron map is simulated by extrapolating the Haslam 408 MHz all-sky map as the template to lower frequencies with a power-law spectrum. We make use of the high-resolution version ($N_{\text{side}} = 2048$, pixel size $\sim 1.72'$) of the Haslam 408 MHz map⁴, which was reprocessed by Remazeilles et al. (2015) us-

³ The 68% uncertainty is derived from the 16th and 84th percentiles because they are more robust than the mean and standard deviation for data with large dispersion.

⁴ The reprocessed Haslam 408 MHz map: http://www.jb.man.ac.uk/research/cosmos/haslam_map/

ing significantly better instrument calibration and more accurate subtraction of extragalactic sources. We also use the all-sky synchrotron spectral index map made by Giardino et al. (2002) to account for the index variation with sky positions. The Galactic free-free emission is deduced from the H α survey data (Finkbeiner 2003), which is corrected for dust absorption, by employing the tight relation between the H α and free-free emissions due to their common origins (see Dickinson et al. 2003, and references therein). Since the Galactic diffuse emissions vary remarkably across the sky, we simulate them at position of (R.A., decl.) = $(0^\circ, -27^\circ)$, which locates at a high galactic latitude ($b = -78.5^\circ$) and is expected to be an appropriate choice for this study (see also Section 3).

The extragalactic point sources are simulated by taking into account the following five types of sources: (1) star-forming and starburst galaxies, (2) radio-quiet AGNs, (3) Fanaroff–Riley type I and type II AGNs, (4) GHz-peaked spectrum AGNs, and (5) compact steep spectrum AGNs. We simulate the former three types of sources by leveraging the simulation results made by Wilman et al. (2008), and simulate the latter two types by employing their corresponding luminosity functions and spectral models. More details can be found in Wang et al. (2010) and references therein.

The rms brightness temperatures of the Galactic synchrotron emission, Galactic free-free emission, and extragalactic point sources are listed in Table 1, and example maps simulated at 158 MHz for these components are shown in Figure 8.

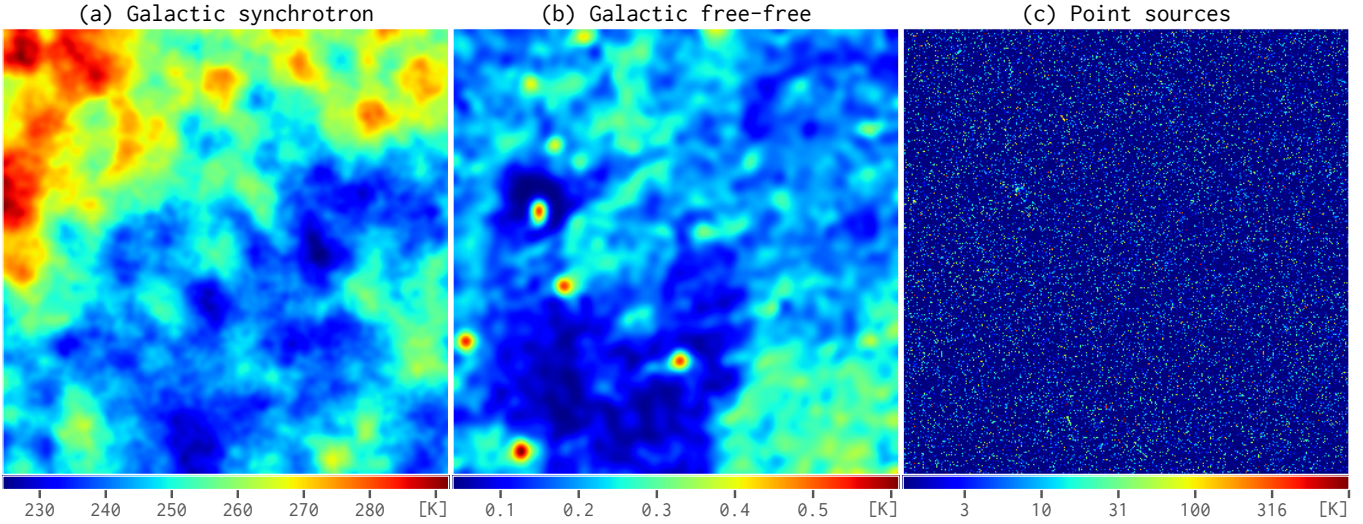
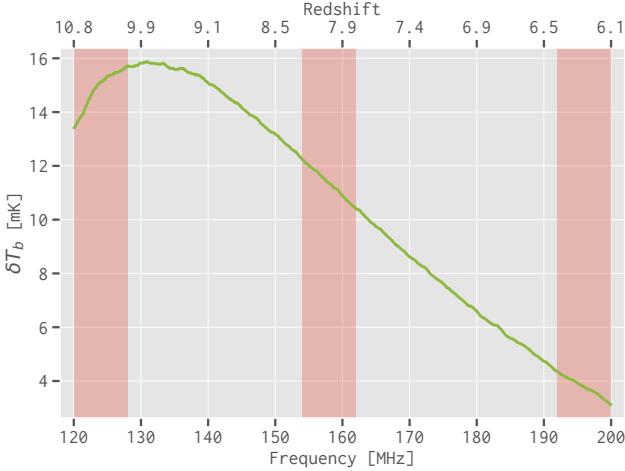
2.3. EoR Signal

The sky maps of the EoR signal are created using the 2016 data release from the *Evolution Of 21 cm Structure* project⁵, which has made use of the 21cmFAST to simulate the cosmic reionization process from redshift 86.5 to 5.0 inside a large cube that is 1.6 comoving Gpc (1024 cells) along each side (Mesinger et al. 2016). We extract the image slices at needed frequencies (i.e., redshifts) from the light-cone cubes of the recommended “faint galaxies” case, and then tile and rescale them to have the same sky coverage and pixel size as our foreground maps. Figure 9 shows the rms brightness temperatures of the EoR signal among 120–200 MHz ($z = 6.1$ –10.8). The corresponding rms brightness temperatures at the central frequencies of the three adopted bands are given in Table 1 and the sky map of the EoR signal at 158 MHz is shown in Figure 10.

⁵ Evolution Of 21 cm Structure project: <http://homepage.sns.it/mesinger/EOS.html>

Table 1. The rms Brightness Temperatures of All Components (unit: mK)

Component	124 MHz	158 MHz	196 MHz
Radio halos (100 simulations)	$(4.21^{+11.2}_{-2.60}) \times 10^3$	$(1.81^{+5.28}_{-1.13}) \times 10^3$	$(0.85^{+2.74}_{-0.54}) \times 10^3$
Galactic synchrotron	4.74×10^5	2.52×10^5	1.43×10^5
Galactic free-free	330	200	130
Point sources	29.7×10^7	5.90×10^7	1.39×10^7
EoR signal	15.1	11.3	3.77

**Figure 8.** The sky maps of (a) the Galactic synchrotron emission, (b) the Galactic free-free emission, and (c) extragalactic point sources at 158 MHz. All the maps cover sky region of size $10^\circ \times 10^\circ$ and have color bars in units of K.**Figure 9.** The rms brightness temperatures of the EoR signal (solid green line) within 120–200 MHz ($z = 6.1\text{--}10.8$). The red-shaded regions mark the three adopted frequency bands (120–128, 154–162, and 192–200 MHz).

3. SIMULATION OF SKA OBSERVATIONS

In order to properly evaluate the contamination of radio halos on the EoR observations, it is essential to take account of the practical instrumental effects of radio interferometers. Therefore, we employ the latest SKA1-Low layout configuration⁶ to simulate the SKA observations of the above sky maps. According to this layout configuration, the SKA1-Low interferometer consists of 512 stations, with 224 of them randomly distributed within the “core” of 1000 m in diameter, while the remaining stations are grouped into “clusters” and placed on three spiral arms extending up to a radius of ~ 35 km. Each station has 256 antennas randomly distributed with a minimum separation of $d_{\min} = 1.5$ m inside a circular region of 35 m in diameter (e.g., Mort *et al.* 2017).

The 8 MHz bandwidth of each frequency band is divided into 51 channels for a frequency resolution of

⁶ SKA1-Low Configuration Coordinates:
https://astronomers.skatelescope.org/wp-content/uploads/2016/09/SKA-TEL-SKO-0000422_02_SKA1_LowConfigurationCoordinates-1.pdf (released on 2016 May 31)

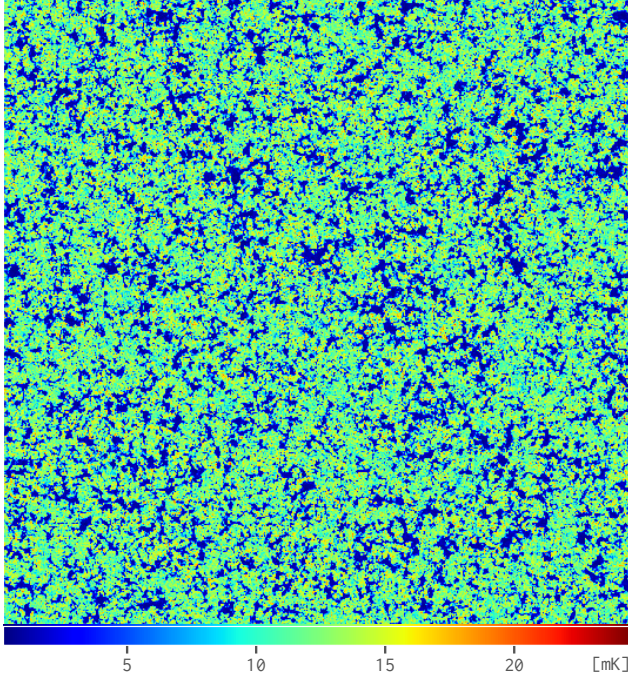


Figure 10. The sky map of the EoR signal at 158 MHz. The sky region size is $10^\circ \times 10^\circ$ and the color bar is in units of mK.

160 kHz. For each component, we simulate the input sky maps at every frequency channel, and then use the OSKAR⁷ simulator (Mort et al. 2010) to perform observations for 6 hr. The input sky maps are centered at sky position of (R.A., decl.) = $(0^\circ, -27^\circ)$, which passes through the zenith of the SKA1-Low telescope and is an ideal choice for the simulation of SKA observations. The simulated visibility data are imaged through the WS Clean⁸ imager (Offringa et al. 2014) using Briggs’ weighting with a robustness of zero (Briggs 1995), and the images created are cropped to keep only the central regions because the marginal regions suffer from the problem of insufficient CLEAN. As the telescope’s field of view (FoV) is inversely proportional to the observing frequency, we choose to keep the central $6^\circ \times 6^\circ$, $5^\circ \times 5^\circ$, and $4^\circ \times 4^\circ$ regions in the 120–128, 154–162, and 192–200 MHz frequency bands, respectively.

The Galactic synchrotron and free-free emissions are combined for the simulated observations because they have similar diffuse features. Similar to the real-time peeling of the brightest point sources in practical data analysis pipelines (e.g., Mitchell et al. 2008; Intema et al. 2009; Mort et al. 2017), we assume that extragalactic point sources with a 158 MHz flux density

$S_{158} > 50$ mJy are removed (e.g., Liu et al. 2009; Pindor et al. 2011). Thus, the rms brightness temperatures of point sources are significantly reduced to be about $(22.5, 9.81,$ and $4.75) \times 10^4$ mK at 124, 158, and 196 MHz, respectively. In addition, we create the foreground image cubes in each frequency band using the CLEAN algorithm with joined-channel deconvolution in order to ensure the spectral smoothness (Offringa & Smirnov 2017), which is crucial to extract the faint EoR signal in the presence of overwhelming foreground contamination. For the EoR signal, we directly use the dirty images because the CLEAN algorithm is not well applicable to such faint and diffuse emissions. Hence we obtain the SKA “observed” image cubes of the EoR signal, radio halos, the Galactic diffuse emission (with synchrotron and free-free emissions combined), and the extragalactic point sources (with the brightest ones removed) in the 120–128, 154–162, and 192–200 MHz frequency bands.

4. POWER SPECTRA AND EOR WINDOW

In order to characterize the contamination of radio halos on the EoR observations in terms of both foreground removal and avoidance methods, we utilize the power spectra and EoR window to compare the powers of radio halos with the EoR signal as well as other foreground components. The redshifted 21 cm signal expected to be observed at different frequencies represents a three-dimensional (3D) data cube, where the two spatial dimensions describe the transverse distances across the sky and the frequency dimension maps to the line-of-sight distance. Within a limited redshift range (e.g., $\Delta z \sim 0.5$, corresponding to a frequency bandwidth of ~ 8 MHz at 158 MHz) during the EoR, the evolution effect of the universe is minor and the H I distribution is believed to be isotropic. The corresponding 3D power spectrum $P(k_x, k_y, k_z)$ of the EoR signal should have spherical symmetry and can be averaged in spherical shells of radii k , yielding the one-dimensional (1D) power spectrum $P(k)$, which effectively increases the signal-to-noise ratio compared to direct imaging observations (Morales & Hewitt 2004; Morales et al. 2006; Datta et al. 2010). The dimensionless variant of the 1D power spectrum $\Delta^2(k) = P(k)k^3/(2\pi^2)$ is more commonly used in the literature. To suppress the significant side lobes in the Fourier transform caused by the sharp discontinuities at the ends of the finite frequency band, we apply the Blackman–Nuttall window function to the frequency dimension before calculating the power spectra (e.g., Trott & Tingay 2015; Chapman et al. 2016).

Since the two angular dimensions and the frequency dimension of the image cubes of foreground continuum emissions are independent, which is different from the

⁷ OSKAR: <https://github.com/OxfordSKA/OSKAR> (v2.7.0)

⁸ WS Clean: <https://sourceforge.net/p/wsclean> (v2.6)

image cube of the redshifted 21 cm signal, it is appropriate to average the 3D power spectrum $P(k_x, k_y, k_z)$ over angular annuli of radii $k_{\perp} \equiv \sqrt{k_x^2 + k_y^2}$ for each line-of-sight plane $k_{\parallel} \equiv k_z$, which yields the two-dimensional (2D) power spectrum $P(k_{\perp}, k_{\parallel})$. In the $(k_{\perp}, k_{\parallel})$ plane, the spectral-smooth foreground emissions are supposed to reside in the low- k_{\parallel} region, although complicated instrumental and observational effects (e.g., chromatic primary beams, calibration errors) can throw some of the foreground contamination from the purely angular (k_{\perp}) modes into the line-of-sight (k_{\parallel}) dimension (i.e., mode mixing), which results in an expanded wedge-like contamination region at the bottom right in the $(k_{\perp}, k_{\parallel})$ plane (i.e., foreground wedge; Datta et al. 2010; Morales et al. 2012; Liu et al. 2014). The region almost free of the foreground contamination, namely the EoR window, is preserved at the top left in the $(k_{\perp}, k_{\parallel})$ plane and is described with

$$k_{\parallel} \geq \frac{H(z)D_M(z)}{(1+z)c} \left[k_{\perp} \sin \Theta + \frac{2\pi w f_{21}}{(1+z)D_M(z)B} \right] \quad (36)$$

(Thyagarajan et al. 2013), where $B = 8$ MHz is the frequency bandwidth of the image cube, $f_{21} = 1420.4$ MHz is the rest-frame frequency of the 21 cm line, $z = f_{21}/f_c - 1$ is the signal redshift corresponding to the central frequency (f_c) of the image cube, $H(z)$ is the Hubble parameter at redshift z [see Equation (A4)], $D_M(z)$ is the transverse comoving distance, w denotes the number of characteristic convolution widths ($\propto B^{-1}$) for the spillover region caused by the variations in instrumental frequency response, and Θ is the angular distance of foreground sources from the field center.

5. RESULTS

We evaluate the contamination of radio halos on the EoR observations for both foreground removal and avoidance methods. First, we calculate the 1D power spectra and compare the powers of radio halos with the EoR signal, which illustrates the impacts of radio halos with the foreground removal methods. Next, we calculate the 2D power spectra and carry out the comparison between radio halos and the EoR signal inside the EoR window, from which we evaluate the effects imposed by radio halos in adopting the foreground avoidance methods to extract the EoR signal.

5.1. 1D Power Spectra

We calculate the 1D dimensionless power spectra $\Delta^2(k)$ for each image cube obtained in Section 3. For radio halos, we make use of all 100 simulation runs (Section 2.1) to estimate the median power spectra and the corresponding 68% uncertainties. The comparisons of

the power spectra $\Delta^2(k)$ between radio halos and the EoR signal in each frequency band are displayed in Figure 11, where we also show the power spectra of Galactic diffuse emission and extragalactic point sources for comparison. The median power spectra (solid red lines) show that radio halos are generally more luminous than the EoR signal by about 10^4 , 10^3 , and $10^{2.5}$ times on scales of $0.1 \text{ Mpc}^{-1} < k < 2 \text{ Mpc}^{-1}$ in the 120–128, 154–162, and 192–200 MHz bands, respectively. Given the large uncertainties in, e.g., brightness and number density, of radio halos, the power spectra can vary by about 10–100 times with respect to the median values within the 68% uncertainties (red-shaded regions). We also find that, although on large scales ($k \lesssim 0.1 \text{ Mpc}^{-1}$) the Galactic foreground is the strongest contaminating source, its power deceases rapidly as the scale becomes smaller and is weaker than the median power of radio halos by a factor of about 10–100 on scales of $0.5 \text{ Mpc}^{-1} \lesssim k \lesssim 1 \text{ Mpc}^{-1}$ in all the three bands. These results evidently show that radio halos are severe foreground contaminating sources. Moreover, it can be a major challenge to accurately model and remove radio halos, due to their diffuse and relatively complicated morphologies.

5.2. 2D Power Spectra

We take the 154–162 MHz band as an example and show in Figure 12 the 2D power spectra $P(k_{\perp}, k_{\parallel})$ of the EoR signal, radio halos (the median power spectrum of the 100 simulation runs), Galactic diffuse emission, and extragalactic point sources. We find that, as shown in many previous works, the EoR signal distributes its power across all k_{\parallel} modes, illustrating its rapid fluctuations along the line-of-sight dimension, while the spectral-smooth foreground components dominate only in the low- k_{\parallel} regions ($k_{\parallel} \lesssim 0.2 \text{ Mpc}^{-1}$). With regard to the angular dimension, the power of radio halos appears in the range of $k_{\perp} \lesssim 1 \text{ Mpc}^{-1}$, showing a concentration on the intermediate scales of $k_{\perp} \sim 0.5 \text{ Mpc}^{-1}$. Meanwhile, the powers of Galactic diffuse emission and extragalactic point sources dominate on the large scales of $k_{\perp} \lesssim 0.1 \text{ Mpc}^{-1}$ and a broad angular scales of $k_{\perp} \gtrsim 0.1 \text{ Mpc}^{-1}$, respectively. These results are also consistent with Figure 11(b).

In order to better evaluate the importance of radio halos as foreground contaminating sources, we calculate the 2D power spectrum ratios $R(k_{\perp}, k_{\parallel})$ that are obtained by dividing the median 2D power spectra of radio halos by those of the EoR signal in each frequency band. We find that, as shown in Figure 13, the EoR measurements will be significantly affected by radio halos on angular scales of $\gtrsim 0.1 \text{ Mpc}^{-1}$, $\gtrsim 0.3 \text{ Mpc}^{-1}$,

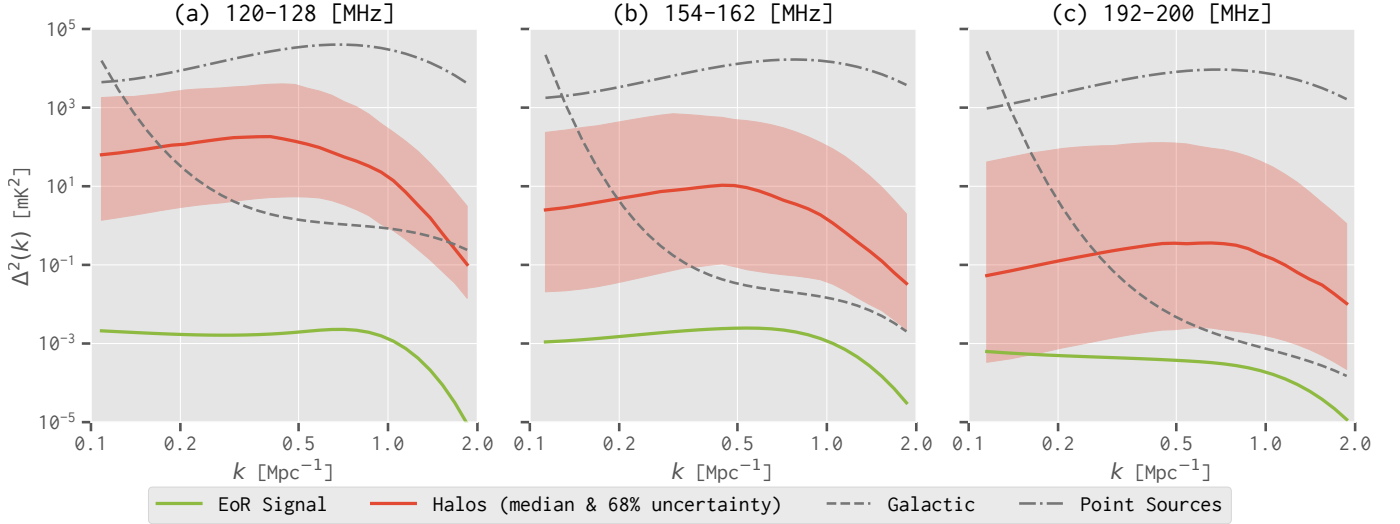


Figure 11. Comparisons of the 1D dimensionless power spectra $\Delta^2(k)$ among the EoR signal (solid green line), radio halos (solid red line), Galactic diffuse emission (dashed gray line), and extragalactic point sources (dashed-dotted gray line) in the (a) 120–128 MHz, (b) 154–162 MHz, and (c) 192–200 MHz frequency bands. The solid red lines and shaded regions represent the median values and the corresponding 68% uncertainties of the power spectra for radio halos estimated from the 100 simulation runs.

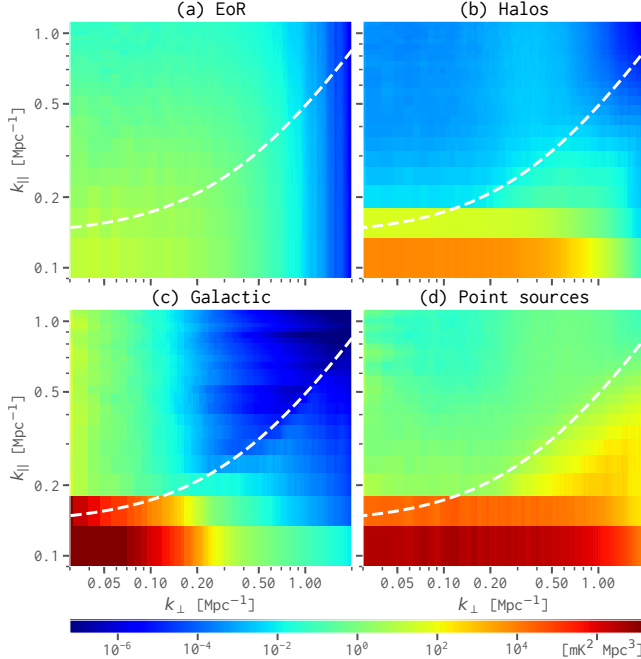


Figure 12. The 154–162 MHz 2D power spectra $P(k_\perp, k_\parallel)$ of (a) the EoR signal, (b) radio halos (median of the 100 simulation runs), (c) Galactic diffuse emission, and (d) extragalactic point sources. All panels share the same logarithmic scale in units of [$\text{mK}^2 \text{Mpc}^3$]. The dashed white lines mark the boundary between the EoR window (at the top left) and the contaminating wedge (at the bottom right).

and $\gtrsim 0.5 \text{ Mpc}^{-1}$ in the 120–128, 154–162, and 192–200 MHz bands, respectively. It is also clearly shown that radio halos turn to cause stronger contamination at

lower frequencies (~ 120 MHz) than at higher frequencies (~ 200 MHz).

To further quantify the contamination caused by radio halos when foreground avoidance methods are applied, we need to appropriately define an EoR window in the (k_\perp, k_\parallel) plane to avoid the heavily contaminated areas and then compare the powers of radio halos and the EoR signal derived inside the window. We have tested multiple parameter configurations (w, Θ) as defined in Equation (36), and find that when $w = 3$ and Θ being about 1.5 times the SKA1-Low’s FoV (i.e., $\Theta = 7.5^\circ, 6.0^\circ$, and 4.8° in 120–128, 154–162, and 192–200 MHz bands, respectively) are used, a conservative EoR window boundary can be defined to well avoid the contaminating wedge (Figures 12 and 13). However, a significant part (about 45%, 46%, and 60% in 120–128, 154–162, and 192–200 MHz bands, respectively) of the power of the EoR signal is lost in the excised wedges. By averaging the modes only inside the defined EoR window, we calculate the 1D power spectrum ratios $R_{\text{eorw}}(k)$ of radio halos to the EoR signal and present the results in Figure 14. We find that, compared to Figure 11, the 1D power ratios inside the EoR window $R_{\text{eorw}}(k)$ are suppressed by about four orders of magnitude, which demonstrates that the EoR window is a powerful tool in detecting the EoR signal. For example, $R_{\text{eorw}}(k)$ on scales of $k \sim 1 \text{ Mpc}^{-1}$ are generally about 45%, 6%, and 2% in the 120–128, 154–162, and 192–200 MHz bands, respectively. However, the power of radio halos leaked into the EoR window can still be significant, considering that $R_{\text{eorw}}(k)$ on

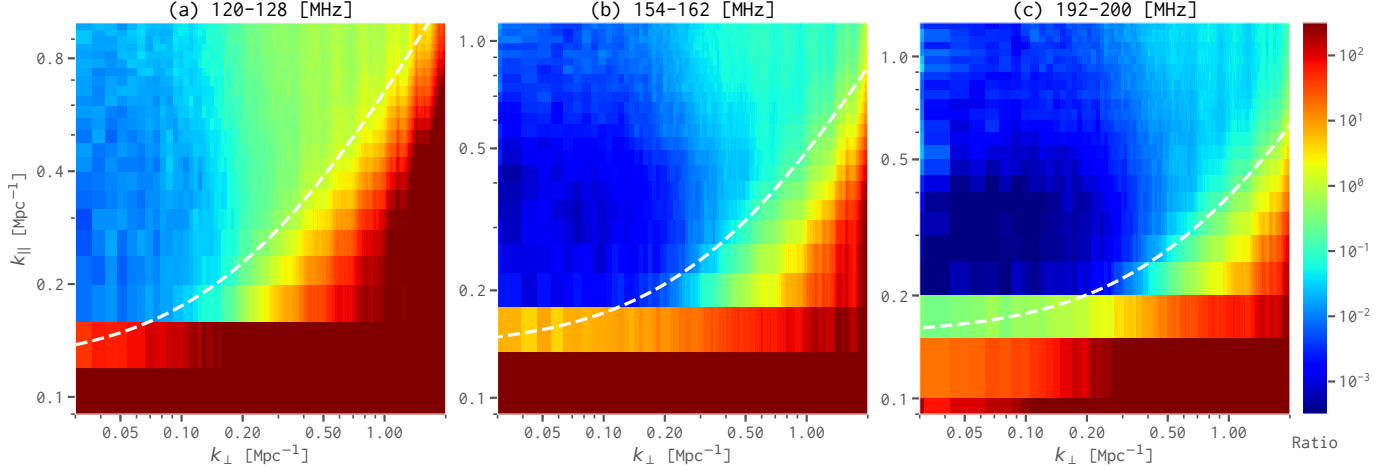


Figure 13. The 2D power spectrum ratios $R(k_{\perp}, k_{\parallel})$ of radio halos to the EoR signal in the (a) 120–128 MHz, (b) 154–162 MHz, and (c) 192–200 MHz frequency bands. The median 2D power spectrum of 100 simulation runs for radio halos is used. All panels use the same color bar in logarithmic scale. The dashed white lines mark the EoR window boundaries.

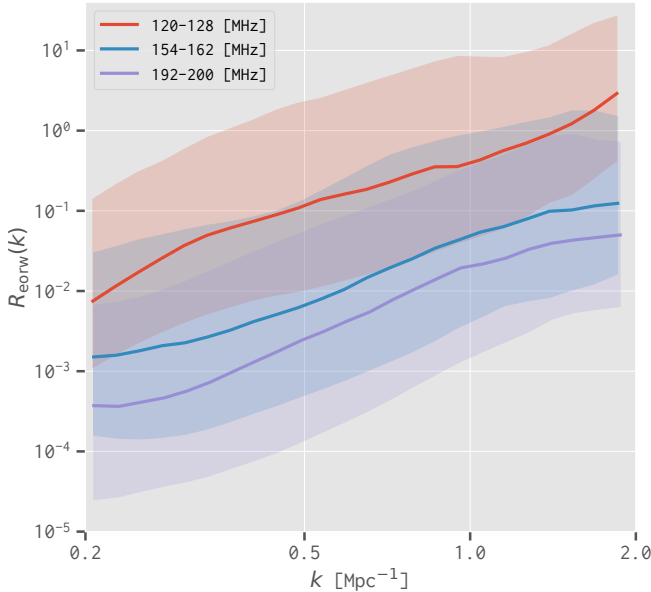


Figure 14. The 1D power ratios $R_{\text{eorw}}(k)$ inside the EoR window of radio halos to the EoR signal. The solid lines and shaded regions show the median values and corresponding 68% uncertainties, respectively.

scales of $0.5 \text{ Mpc}^{-1} \lesssim k \lesssim 1 \text{ Mpc}^{-1}$ can be up to about 230–800%, 18–95%, and 7–40% in the three frequency bands within the 68% uncertainties (shaded regions).

Based on the above results, we conclude that radio halos are severe foreground contaminating sources to EoR observations. Even inside the EoR window where most of the strong foreground contamination is avoided, radio halos can still imprint non-negligible contamination on the EoR measurements, especially at lower frequencies ($\sim 120 \text{ MHz}$). Careful treatments of radio halos as well as other foreground contaminating sources would

be indispensable for obtaining an EoR window that is not only sufficiently clean but also as large as possible to preserve maximum information of the EoR signal.

6. DISCUSSION

In practical observations with low-frequency radio interferometers, the situations are much more complicated than our simulations. For example, calibration uncertainties (e.g., insufficient sky modeling) as well as other complicated instrumental and observational effects (e.g., cable signal reflections, ionospheric distortions) can cause frequency artifacts in the derived image cubes. Foreground sources located in the side lobes of the station beam can also significantly reduce the imaging dynamical range and quality. In this section, we investigate how the EoR measurements are affected in these two situations if the contamination of radio halos is not properly removed.

6.1. Impacts of Frequency Artifacts

The smoothness along the frequency dimension is the most crucial feature of various foreground components and is the key to extract the faint EoR signal. However, frequency artifacts may present in the obtained image cubes due to calibration uncertainties and various instrumental and observational effects, which break the spectral smoothness of the foreground emission and hence damage the EoR measurements.

To evaluate the influence of the frequency artifacts on the power spectra, we multiply each slice of the image cube by a random number drawn from a Gaussian distribution with unity mean and then compare the resulting power spectra (Chapman *et al.* 2016). Some simulation and observation studies have suggested that the residual calibration errors in frequency channels may be

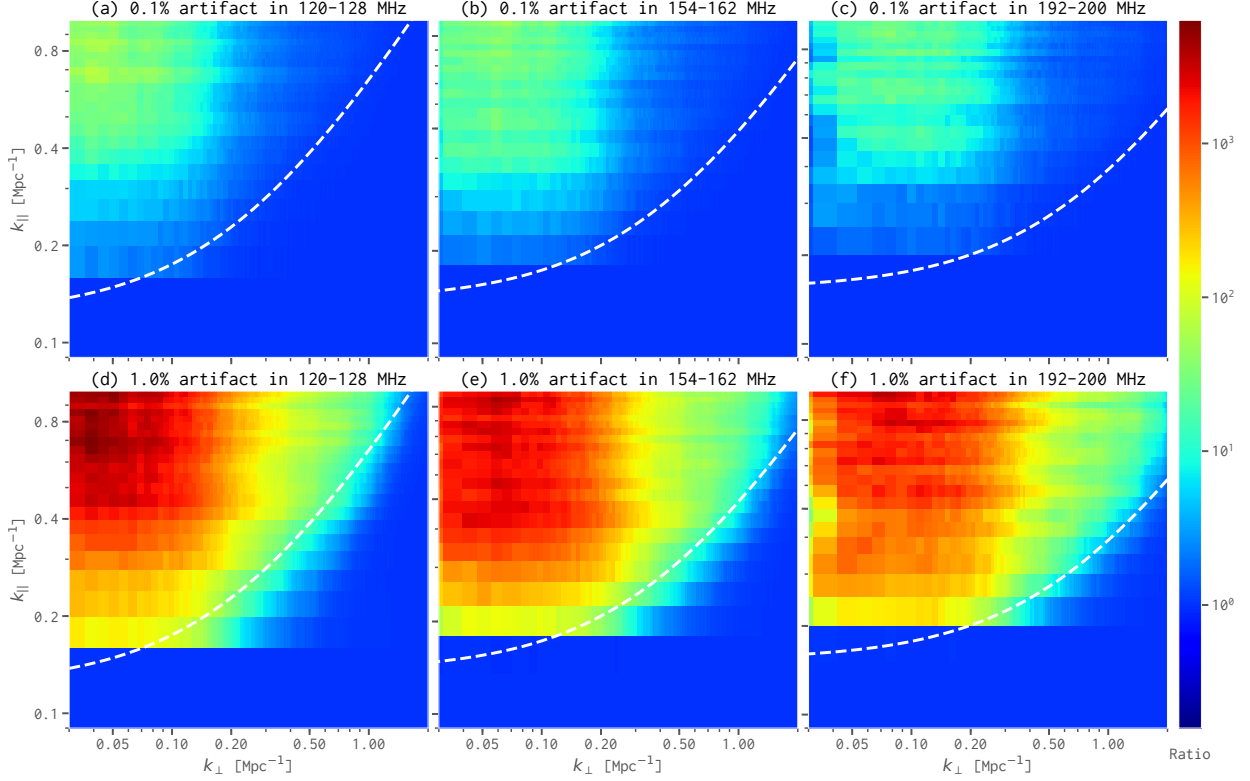


Figure 15. The 2D power spectrum ratios $R_{\text{arti}}(k_{\perp}, k_{\parallel})$ of radio halos that are obtained between the modified image cubes with frequency artifacts and the original ones. All the 100 simulation runs for radio halos are used to derive the median 2D power spectrum ratios that are presented here. The upper and lower rows show the cases of frequency artifacts being $A_{\text{arti}} = 0.1\%$ and $A_{\text{arti}} = 1\%$, respectively. The left, middle, and right columns show the power spectrum ratios in the 120–128, 154–162, and 192–200 MHz bands, respectively. The dashed white lines mark the EoR window boundaries. All panels share the same color bar in logarithmic scale.

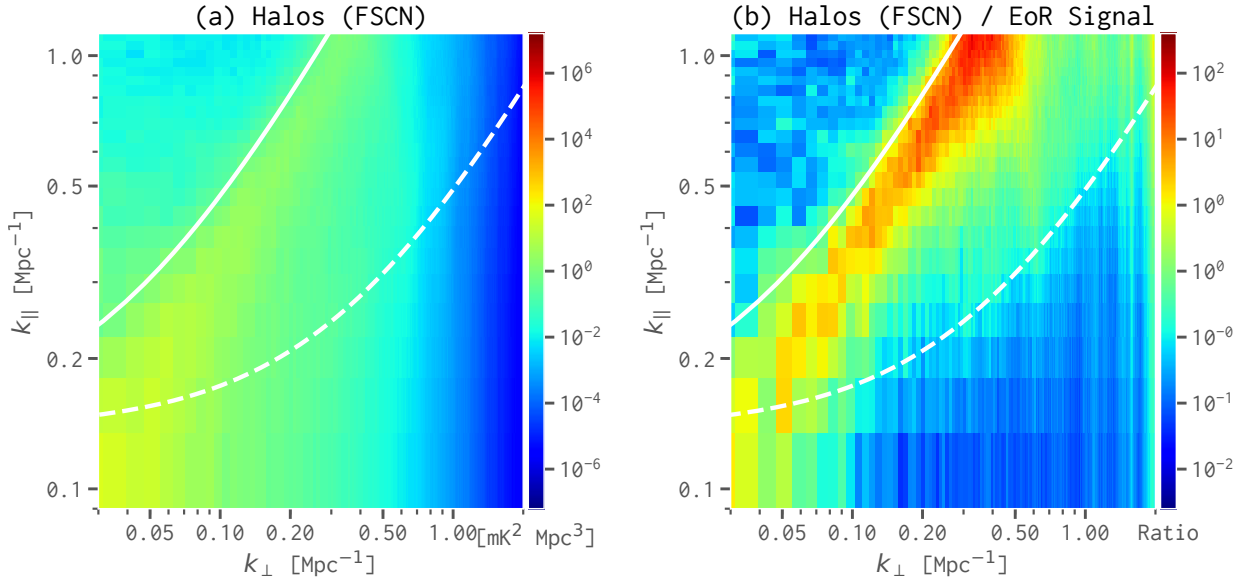


Figure 16. (a) The 2D power spectrum of the FSCN caused by radio halos in the far side lobes of the station beam. (b) The 2D power spectrum ratio of the FSCN to the EoR signal. The results are derived in the 154–162 MHz band. The dashed and solid white lines mark the EoR window boundaries defined with $\Theta = 6^\circ$ and 90° , respectively.

about 0.1%–1% (e.g., Barry et al. 2016; Beardsley et al. 2016; Ewall-Wice et al. 2017). We thus investigate two extreme cases here: a frequency artifact of amplitude $A_{\text{arti}} = 0.1\%$ by using $\sigma = 0.001$ for the Gaussian distribution and a frequency artifact of $A_{\text{arti}} = 1\%$ with $\sigma = 0.01$.

For each of the 100 simulation runs for radio halos, we calculate the 2D power spectrum ratios $R_{\text{arti}}(k_{\perp}, k_{\parallel})$ of the modified image cube with the frequency artifact to the original one (Section 3), and present the median 2D power spectrum ratios obtained in the 120–128, 154–162, and 192–200 MHz bands with either $A_{\text{arti}} = 0.1\%$ or 1% in Figure 15. We find that, when the frequency artifact is added, the resulting 2D power spectra are seriously damaged in all three frequency bands. On scales of $k_{\perp} \lesssim 0.2 \text{ Mpc}^{-1}$ and $k_{\parallel} \gtrsim 0.3 \text{ Mpc}^{-1}$, adding frequency artifact of $A_{\text{arti}} = 0.1\%$ causes the power of radio halos to be about 17, 15, and 13 times stronger in the 120–128, 154–162, and 192–200 MHz bands, respectively, and the corresponding power increases are about 1700, 1500, and 1300 times for frequency artifact of $A_{\text{arti}} = 1\%$. As a comparison, we add the same frequency artifacts ($A_{\text{arti}} = 0.1\%$ and 1%) to the image cubes of the EoR signal, but find that the changes in the calculated 2D power spectra are negligible. This is because the EoR signal already fluctuates remarkably along the frequency dimension. Consequently, even very minor ($\sim 0.1\%$) instrumental or calibration errors can make the contamination of radio halos become much stronger, particularly inside the critical EoR window. These results further support our conclusion made in Section 5.2 that radio halos are important foreground sources and must be carefully dealt with in EoR experiments.

6.2. Impacts of Far Side Lobes

Phased arrays, which are widely used in low-frequency radio interferometers (e.g., LOFAR, MWA, SKA1-Low), usually have complicated beam profiles. Sources far from the main lobe of the station beam can introduce noise-like corruptions, known as the far side-lobe confusion noise (FSCN; Smirnov et al. 2012), to images through the multitude of side lobes. FSCN will not decrease once the uv coverage of the observation no longer improves, and can be the limiting factor in the noise performance of interferometers (Mort et al. 2017).

To investigate the impacts of FSCN contributed by the radio halos located in the far side lobes of the station beam, we have generated the corresponding sky model for the OSKAR simulator, which evaluates the radio interferometer measurement equation (Smirnov 2011) and is able to perform full-sky simulations with realistic beam

profiles. More details about the beam shapes and side-lobe properties of the SKA1-Low can be found in Mort et al. (2017). As an example, we simulate the radio halos in the 154–162 MHz band that cover the sky from the edge of the second side lobe ($\phi \sim 10^\circ$ from the field center) to the horizon ($\phi = 90^\circ$). This emulates an ideal CLEAN procedure in practical data analysis that removes all the radio halos in both the main lobe and the first side lobe but leaves the ones in the far side lobes. Using the OSKAR simulator and the `WSClean` imager as described in Section 3, we obtain the dirty images of the central $5^\circ \times 5^\circ$ region and then calculate the 2D power spectrum.

In Figure 16, we present the 2D power spectrum of the FSCN contributed by radio halos and the corresponding 2D power spectrum ratio of the FSCN to the EoR signal. We find that the FSCN contamination is very strong as its power can be about 20 times the power of the EoR signal on scales of $k_{\perp} \sim 0.3 \text{ Mpc}^{-1}$ and $k_{\parallel} \sim 1.0 \text{ Mpc}^{-1}$. The wedge-shaped contamination region moves toward the top left in the $(k_{\perp}, k_{\parallel})$ plane and greatly reduces the EoR window. In order to effectively avoid the FSCN contamination, we are forced to employ a much more conservative EoR window boundary, such as the one defined with $\Theta = 90^\circ$ as marked in Figure 16 with solid white line, at the cost of losing a remarkably larger portion of the EoR signal. In consequence, the serious FSCN contamination makes the selection of EoR sky region a more challenging task since, in principle, neither bright radio halos nor other strong sources are allowed in both the main and side lobes. A highly accurate foreground model is hence crucial to mitigate the impacts of FSCN.

7. SUMMARY

Based on the Press–Schechter formalism and merger-induced turbulent reacceleration model, we have simulated the emission maps of radio halos, for which we have incorporated the SKA1-Low’s instrumental effects by utilizing its latest layout configuration. By carrying out detailed comparisons of power spectra between radio halos and the EoR signal as well as the Galactic diffuse emission and extragalactic point sources in the 120–128, 154–162, and 192–200 MHz bands, we have shown that radio halos are severe contaminating sources, especially toward lower frequencies ($\sim 120 \text{ MHz}$). Even inside the properly defined EoR windows, radio halos can still be non-negligible contaminating sources to EoR observations. Moreover, we have investigated the contamination resulted from frequency artifacts and radio halos located inside the far side lobes, both of which support our conclusion that radio halos are severe foreground

contaminating sources and need careful treatments in the forthcoming deep EoR observations.

We gratefully acknowledge the reviewer for the constructive comments that greatly help improve the manuscript. We would like to thank Fred Dulwich for providing the latest SKA1-Low layout configuration as well as guidance on using the `OSKAR` simulator, André Offringa for help on interferometric imaging with `WSClean`, Mathieu Remazeilles for providing the high-resolution Haslam 408 MHz Galactic synchrotron map, and Giovanna Giardino for the all-sky Galactic synchrotron spectral index map. We also acknowledge Emma Chapman, Uri Keshet, and Abhirup Datta for their help. Part of the work involving `OSKAR` and `WSClean` was performed on the high-performance clus-

ters at Department of Astronomy, Shanghai Jiao Tong University and at Shanghai Astronomical Observatory, Chinese Academy of Sciences. This work is supported by the Ministry of Science and Technology of China (grant Nos. 2018YFA0404601, 2017YFF0210903) and the National Natural Science Foundation of China (grant Nos. 11433002, 11621303, 11835009, 61371147).

Software: `OSKAR` (Mort et al. 2010), `WSClean` (Offringa et al. 2014), `AstroPy` (Astropy Collaboration et al. 2013), `HEALPix` (Górski et al. 2005), `HMF` (Murray et al. 2013), `IPython` (<https://ipython.org/>), `Matplotlib` (<https://matplotlib.org/>), `NumPy` (<http://www.numpy.org/>), `SciPy` (<https://scipy.org/>), `Pandas` (<https://pandas.pydata.org/>), `Engauge Digitizer` (<https://github.com/markummitchell/engauge-digitizer>).

APPENDIX

A. SUPPLEMENTAL FORMULAS

In a flat Λ CDM cosmology as adopted in this work, the critical linear overdensity as a function of redshift z is (Kitayama & Suto 1996; Randall et al. 2002)

$$\delta_c(z) = \frac{D(z=0)}{D(z)} \frac{3}{20} (12\pi)^{2/3} [1 + 0.0123 \log_{10} \Omega_f(z)], \quad (\text{A1})$$

where $\Omega_f(z)$ is the mass density ratio at redshift z defined as

$$\Omega_f(z) = \frac{\Omega_m(1+z)^3}{\Omega_m(1+z)^3 + \Omega_\Lambda}, \quad (\text{A2})$$

and $D(z)$ is the growth factor given by (Peebles 1980, equation (13.6))

$$D(x) = \frac{(x^3 + 2)^{1/2}}{x^{3/2}} \int_0^x y^{3/2} (y^3 + 2)^{-3/2} dy, \quad (\text{A3})$$

with $x_0 \equiv (2\Omega_\Lambda/\Omega_m)^{1/3}$ and $x = x_0/(1+z)$.

The Hubble parameter at redshift z is

$$H(z) = H_0 E(z) = H_0 \sqrt{\Omega_m(1+z)^3 + \Omega_\Lambda}, \quad (\text{A4})$$

where $E(z)$ is the redshift evolution factor (Hogg 1999).

The virial radius of a galaxy cluster at a redshift of z is given by

$$r_{\text{vir}} = \left[\frac{3M_{\text{vir}}}{4\pi \Delta_{\text{vir}}(z) \rho_{\text{crit}}(z)} \right]^{1/3}, \quad (\text{A5})$$

where M_{vir} is the virial mass of the cluster, $\rho_{\text{crit}}(z) = 3H^2(z)/(8\pi G)$ is the critical density, G being the gravitational constant, and $\Delta_{\text{vir}}(z)$ is the virial overdensity given by (e.g., Bryan & Norman 1998)

$$\Delta_{\text{vir}}(z) = 18\pi^2 + 82x - 39x^2, \quad (\text{A6})$$

where $x \equiv \Omega_f(z) - 1$.

B. COLLECTION OF CURRENTLY OBSERVED RADIO HALOS

Table B1. Currently Observed 71 Radio Halos and 9 Candidates (As of 2018 January)

Cluster	Redshift	kpc/''	Size	$S_{1.4\text{ GHz}}$	$P_{1.4\text{ GHz}}$	Notes	References
(1)	(2)	(3)	(4)	(5)	(6)	(7)	(8)
1E 0657–56	0.2960	4.38	1.48	78.0 ± 5.0	21.33 ± 1.49		Liang et al. (2000)
Abell 141	0.2300	3.64	1.20	$1.3 \pm 0.1^{\text{a}}$	0.25 ± 0.02		Duchesne et al. (2017)
Abell 209	0.2060	3.34	1.40	16.9 ± 1.0	2.04 ± 0.12	+cR	Giovannini et al. (2009)
Abell 399	0.0718	1.35	0.57	16.0 ± 2.0	0.20 ± 0.03		Murgia et al. (2010)
Abell 401	0.0737	1.38	0.49	17.0 ± 1.0	0.20 ± 0.01		Bacchi et al. (2003)
Abell 520	0.1990	3.25	0.99	34.4 ± 1.5	3.17 ± 0.14		Govoni et al. (2001)
Abell 521	0.2533	3.91	1.17	5.9 ± 0.5	1.12 ± 0.09	+R	Giovannini et al. (2009)
Abell 523	0.1000	1.82	1.30	59.0 ± 5.0	1.47 ± 0.12		Giovannini et al. (2011)
Abell 545	0.1540	2.64	0.81	23.0 ± 1.0	1.25 ± 0.05		Bacchi et al. (2003)
Abell 665	0.1818	3.03	1.66	43.1 ± 2.2	3.28 ± 0.17		Giovannini & Feretti (2000)
Abell 697	0.2820	4.23	0.75	5.2 ± 0.5	2.20 ± 0.21		van Weeren et al. (2011)
Abell 746	0.2320	3.67	0.85	18.0 ± 4.0	3.80 ± 0.84	+R	van Weeren et al. (2011)
Abell 754	0.0542	1.04	0.95	86.0 ± 4.0	0.56 ± 0.03	+R	Bacchi et al. (2003)
Abell 773	0.2170	3.48	1.13	12.7 ± 1.3	1.39 ± 0.14		Govoni et al. (2001)
Abell 781	0.3004	4.42	1.60	20.5 ± 5.0	5.90 ± 1.44	+cR	Govoni et al. (2011)
Abell 800	0.2223	3.55	1.28	10.6 ± 0.9	1.52 ± 0.13		Govoni et al. (2012)
Abell 851	0.4069	5.40	1.08	3.7 ± 0.3	2.14 ± 0.17		Giovannini et al. (2009)
Abell 1132	0.1369	2.39	0.74	3.3 ± 1.5	0.16 ± 0.07		Wilber et al. (2018)
Abell 1213	0.0469	0.91	0.22	72.2 ± 3.5	0.36 ± 0.02		Giovannini et al. (2009)
Abell 1300	0.3100	4.52	0.92	20.0 ± 2.0	2.99 ± 0.30	+R	Reid et al. (1999)
Abell 1351	0.3220	4.64	1.08	$32.4 \pm \dots$	$11.37 \pm \dots$		Giacintucci et al. (2009b)
Abell 1443	0.2700	4.10	1.10	$11.0 \pm 1.1^{\text{b}}$	2.53 ± 0.30	cH	Bonafede et al. (2015)
Abell 1451	0.1989	3.25	0.74	5.4 ± 0.5	0.62 ± 0.07	+cR	Cuciti et al. (2018)
Abell 1550	0.2540	3.92	1.41	7.7 ± 1.6	1.49 ± 0.31		Govoni et al. (2012)
Abell 1656	0.0232	0.46	0.58	530.0 ± 50.0	0.31 ± 0.03	+cR	Kim et al. (1990)
Abell 1682	0.2272	3.61	0.85	$2.3 \pm 0.5^{\text{c}}$	0.41 ± 0.08	cH	Macario et al. (2013)
Abell 1689	0.1832	3.05	0.73	10.0 ± 2.9	0.92 ± 0.27		Vacca et al. (2011)
Abell 1758A	0.2790	4.20	0.63	3.9 ± 0.4	0.93 ± 0.10	+R	Giovannini et al. (2009)
Abell 1914	0.1712	2.88	1.16	64.0 ± 3.0	4.32 ± 0.20		Bacchi et al. (2003)
Abell 1995	0.3186	4.61	0.83	4.1 ± 0.7	1.35 ± 0.23		Giovannini et al. (2009)
Abell 2034	0.1130	2.03	0.60	7.3 ± 2.0	0.28 ± 0.08	+R	van Weeren et al. (2011)
Abell 2061	0.0784	1.46	1.68	16.9 ± 4.2	0.25 ± 0.06	+R	Farnsworth et al. (2013)
Abell 2065	0.0726	1.36	1.08	32.9 ± 11.0	0.41 ± 0.14		Farnsworth et al. (2013)
Abell 2069	0.1160	2.08	0.90	$6.2 \pm 2.2^{\text{d}}$	0.25 ± 0.05		Drabent et al. (2015)
Abell 2142	0.0909	1.67	0.99	11.8 ± 0.8	1.12 ± 0.08		Venturi et al. (2017)
Abell 2163	0.2030	3.31	2.04	155.0 ± 2.0	14.93 ± 0.20	+R	Feretti et al. (2001)
Abell 2218	0.1710	2.88	0.35	4.7 ± 0.1	0.32 ± 0.01		Giovannini & Feretti (2000)
Abell 2219	0.2256	3.59	1.54	81.0 ± 4.0	9.72 ± 0.48		Bacchi et al. (2003)
Abell 2254	0.1780	2.98	0.85	33.7 ± 1.8	2.43 ± 0.13		Govoni et al. (2001)
Abell 2255	0.0806	1.50	0.90	56.0 ± 3.0	0.87 ± 0.05	+R	Govoni et al. (2005)
Abell 2256	0.0594	1.13	0.81	103.4 ± 1.1	0.82 ± 0.01	+R	Clarke & Ensslin (2006)
Abell 2294	0.1780	2.98	0.54	5.8 ± 0.5	0.51 ± 0.04		Giovannini et al. (2009)
Abell 2319	0.0524	1.01	0.93	153.0 ± 8.0	0.54 ± 0.03		Feretti et al. (1997)
Abell 2680	0.1901	3.14	0.57	$1.8 \pm 0.6^{\text{e}}$	0.16 ± 0.05	cH	Duchesne et al. (2017)
Abell 2693	0.1730	2.91	0.65	$7.7 \pm 0.9^{\text{f}}$	0.61 ± 0.07	cH	Duchesne et al. (2017)
Abell 2744	0.3080	4.50	1.62	57.1 ± 2.9	12.89 ± 0.65	+R	Govoni et al. (2001)

Table B1 continued

Table B1 (*continued*)

Cluster	Redshift	kpc/''	Size	$S_{1.4 \text{ GHz}}$	$P_{1.4 \text{ GHz}}$	Notes	References
(1)	(2)	(3)	(4)	(5)	(6)	(7)	(8)
Abell 2811	0.1080	1.95	0.48	3.4 ± 0.7^g	0.10 ± 0.02		Duchesne et al. (2017)
Abell 3411	0.1687	2.85	0.90	4.8 ± 0.5	0.46 ± 0.05	+R	van Weeren et al. (2013)
Abell 3562	0.0480	0.93	0.44	20.0 ± 2.0	0.10 ± 0.01		Venturi et al. (2003)
Abell 3888	0.1510	2.60	0.99	27.6 ± 3.1	1.85 ± 0.19		Shakouri et al. (2016)
Abell S84	0.1080	1.95	0.49	2.1 ± 0.3^h	0.06 ± 0.01	cH	Duchesne et al. (2017)
Abell S1121	0.3580	4.98	1.25	9.8 ± 3.1^h	4.54 ± 1.44		Duchesne et al. (2017)
ACT-CL J0102–4915	0.8700	7.73	2.17	10.7 ± 1.1^i	44.43 ± 1.28	+2R	Lindner et al. (2014)
ACT-CL J0256.5+0006	0.3430	4.84	0.79	2.1 ± 0.5^i	0.97 ± 0.29		Knowles et al. (2016)
CIZA J0107.7+5408	0.1066	1.93	1.10	55.0 ± 5.0	1.80 ± 0.16		van Weeren et al. (2011)
CIZA J0638.1+4747	0.1740	2.92	0.59	3.6 ± 0.2	0.30 ± 0.02		Cuciti et al. (2018)
CIZA J1938.3+5409	0.2600	3.99	0.72	1.6 ± 0.2^b	0.36 ± 0.05		Bonafede et al. (2015)
CIZA J2242.8+5301	0.1921	3.16	1.77	33.5 ± 6.2^j	3.40 ± 0.97	+2R	Govoni et al. (2012)
CIG 0016+16	0.5456	6.37	0.77	$5.5 \pm \dots$	$4.42 \pm \dots$		Giovannini & Feretti (2000)
CIG 0217+70	0.0655	1.24	0.73	58.6 ± 0.9	0.54 ± 0.01	+2R	Brown et al. (2011)
CIG 1446+26	0.3700	5.09	1.22	7.7 ± 2.6	3.57 ± 1.21	+R	Govoni et al. (2012)
CIG 1821+64	0.2990	4.41	1.10	13.0 ± 0.8^k	3.70 ± 0.10		Bonafede et al. (2014b)
MACS J0416.1–2403	0.3960	5.31	0.64	1.7 ± 0.8^l	1.26 ± 0.29		Pandey-Pommier et al. (2015)
MACS J0520.7–1328	0.3400	4.81	0.80	9.0 ± 1.6	3.38 ± 0.60	+cH	Macario et al. (2014)
MACS J0553.4–3342	0.4070	5.40	1.32	9.2 ± 0.7^b	6.73 ± 0.61		Bonafede et al. (2012)
MACS J0717.5+3745	0.5458	6.37	1.20	118.0 ± 5.0	50.00 ± 10.00	+R	van Weeren et al. (2009)
MACS J0949.8+1708	0.3825	5.20	1.04	3.1 ± 0.3^b	1.63 ± 0.15		Bonafede et al. (2015)
MACS J1149.5+2223	0.5444	6.36	1.32	1.2 ± 0.5	1.95 ± 0.93	+cH, +2R	Bonafede et al. (2012)
MACS J1752.0+4440	0.3660	5.05	1.65	14.2 ± 1.4^{m}	9.50 ± 0.91	+2R	van Weeren et al. (2012)
MACS J2243.3–0935	0.4470	5.71	0.91	3.1 ± 0.6^n	3.11 ± 0.58	+cR	Cantwell et al. (2016)
PLCK G147.3–16.6	0.6500	6.92	1.80	2.5 ± 0.4^o	5.10 ± 0.80		van Weeren et al. (2014)
PLCK G171.9–40.7	0.2700	4.10	0.99	18.0 ± 2.0	4.76 ± 0.10		Giacintucci et al. (2013)
PLCK G285.0–23.7	0.3900	5.26	0.73	2.9 ± 0.4^p	1.67 ± 0.21		Martinez Aviles et al. (2016)
PLCK G287.0+32.9	0.3900	5.26	1.30	8.8 ± 0.9	5.10 ± 0.51	+2R	Bonafede et al. (2014a)
PSZ1 G108.18–11.53	0.3347	4.77	0.84	6.8 ± 0.2	2.72 ± 0.10	+2R	de Gasperin et al. (2015)
RXC J1234.2+0947	0.2290	3.63	0.92	$2.0 \pm \dots$	$0.30 \pm \dots$	cH	Govoni et al. (2012)
RXC J1314.4–2515	0.2474	3.85	1.27	20.3 ± 0.8	1.45 ± 0.06	+2R	Feretti et al. (2005)
RXC J1514.9–1523	0.2226	3.55	1.38	10.0 ± 2.0	1.65 ± 0.33		Giacintucci et al. (2011)
RXC J2003.5–2323	0.3171	4.59	1.38	35.0 ± 2.0	11.96 ± 0.68		Giacintucci et al. (2009a)
RXC J2351.0–1954	0.2477	3.85	0.64	4.5 ± 0.9^q	0.89 ± 0.18	+cH	Duchesne et al. (2017)

NOTE—(a) Extrapolated from 168 MHz with spectral index $\alpha = 2.1$; (b) Extrapolated from 323 MHz with spectral index $\alpha = 1.3$; (c) Extrapolated from 153 MHz with spectral index $\alpha = 1.7$; (d) Extrapolated from 346 MHz with spectral index $\alpha = 1.0$; (e) Extrapolated from 168 MHz with spectral index $\alpha = 1.2$; (f) Extrapolated from 168 MHz with spectral index $\alpha = 0.88$; (g) Extrapolated from 168 MHz with spectral index $\alpha = 1.5$; (h) Extrapolated from 168 MHz with spectral index $\alpha = 1.3$; (i) Extrapolated from 610 MHz with spectral index $\alpha = 1.2$; (j) Extrapolated from 145 MHz with spectral index $\alpha = 1.03$; (k) Extrapolated from 325 MHz with spectral index $\alpha = 1.04$; (l) Extrapolated from 340 MHz with spectral index $\alpha = 1.5$; (m) Extrapolated from 1714 MHz with spectral index $\alpha = 1.1$; (n) Extrapolated from 610 MHz with spectral index $\alpha = 1.4$; (o) Extrapolated from 610 MHz with spectral index $\alpha = 1.3$; (p) Extrapolated from 1867 MHz with spectral index $\alpha = 1.3$; (q) Extrapolated from 168 MHz with spectral index $\alpha = 1.4$.

Columns: (1) galaxy cluster name; (2) redshift; (3) kpc per arcsec at the cluster's redshift (converted to our adopted cosmology); (4) largest linear size of the radio halo, in units of Mpc; (5) 1.4 GHz flux density; (6) 1.4 GHz radio power (converted to our adopted cosmology); (7) additional notes (cH, halo candidate; +R, with single relic; +cR, with single relic candidate; +2R, with double relics); (8) references to the quoted properties.

REFERENCES

- Astropy Collaboration, Robitaille, T. P., Tollerud, E. J., et al. 2013, [A&A](#), 558, A33
- Bacchi, M., Feretti, L., Giovannini, G., & Govoni, F. 2003, [A&A](#), 400, 465
- Barry, N., Hazelton, B., Sullivan, I., Morales, M. F., & Pober, J. C. 2016, [MNRAS](#), 461, 3135
- Basu, K. 2012, [MNRAS](#), 421, L112

- Beardsley, A. P., Hazelton, B. J., Sullivan, I. S., et al. 2016, *ApJ*, 833, 102
- Beck, R., & Krause, M. 2005, *Astronomische Nachrichten*, 326, 414
- Blasi, P., Gabici, S., & Brunetti, G. 2007, *International Journal of Modern Physics A*, 22, 681
- Bonafede, A., Intema, H. T., Brüggen, M., et al. 2014a, *ApJ*, 785, 1
- Bonafede, A., Brüggen, M., van Weeren, R., et al. 2012, *MNRAS*, 426, 40
- Bonafede, A., Intema, H. T., Brüggen, M., et al. 2014b, *MNRAS*, 444, L44
- Bonafede, A., Intema, H., Brüggen, M., et al. 2015, *MNRAS*, 454, 3391
- Bond, J. R., Cole, S., Efstathiou, G., & Kaiser, N. 1991, *ApJ*, 379, 440
- Bowman, J. D., Cairns, I., Kaplan, D. L., et al. 2013, *PASA*, 30, e031
- Briggs, D. S. 1995, PhD thesis, The New Mexico Institute of Mining and Technology
- Brown, S., Duesterhoeft, J., & Rudnick, L. 2011, *ApJL*, 727, L25
- Brunetti, G., Blasi, P., Cassano, R., & Gabici, S. 2004, *MNRAS*, 350, 1174
- Brunetti, G., Cassano, R., Dolag, K., & Setti, G. 2009, *A&A*, 507, 661
- Brunetti, G., & Jones, T. W. 2014, *International Journal of Modern Physics D*, 23, 1430007
- Brunetti, G., & Lazarian, A. 2007, *MNRAS*, 378, 245
- . 2011, *MNRAS*, 410, 127
- Brunetti, G., Setti, G., Feretti, L., & Giovannini, G. 2001, *MNRAS*, 320, 365
- Bryan, G. L., & Norman, M. L. 1998, *ApJ*, 495, 80
- Cantwell, T. M., Scaife, A. M. M., Oozeer, N., Wen, Z. L., & Han, J. L. 2016, *MNRAS*, 458, 1803
- Cassano, R., & Brunetti, G. 2005, *MNRAS*, 357, 1313
- Cassano, R., Brunetti, G., Giocoli, C., & Ettori, S. 2016, *A&A*, 593, A81
- Cassano, R., Brunetti, G., Norris, R. P., et al. 2012, *A&A*, 548, A100
- Cassano, R., Brunetti, G., Setti, G., Govoni, F., & Dolag, K. 2007, *MNRAS*, 378, 1565
- Cassano, R., Ettori, S., Brunetti, G., et al. 2013, *ApJ*, 777, 141
- Cassano, R., Bernardi, G., Brunetti, G., et al. 2015, *Advancing Astrophysics with the Square Kilometre Array (AASKA14)*, 73
- Cavaliere, A., & Fusco-Femiano, R. 1976, *A&A*, 49, 137
- Cavaliere, A., Menci, N., & Tozzi, P. 1998, *ApJ*, 501, 493
- Chang, J. S., & Cooper, G. 1970, *Journal of Computational Physics*, 6, 1
- Chapman, E., Zaroubi, S., Abdalla, F. B., et al. 2016, *MNRAS*, 458, 2928
- Clarke, T. E., & Ensslin, T. A. 2006, *AJ*, 131, 2900
- Cuciti, V., Brunetti, G., van Weeren, R., et al. 2018, *A&A*, 609, A61
- Datta, A., Bowman, J. D., & Carilli, C. L. 2010, *ApJ*, 724, 526
- Dayal, P., & Ferrara, A. 2018, *PhR*, 780, 1
- de Gasperin, F., Intema, H. T., van Weeren, R. J., et al. 2015, *MNRAS*, 453, 3483
- DeBoer, D. R., Parsons, A. R., Aguirre, J. E., et al. 2017, *PASP*, 129, 045001
- Di Matteo, T., Ciardi, B., & Miniati, F. 2004, *MNRAS*, 355, 1053
- Dickinson, C., Davies, R. D., & Davis, R. J. 2003, *MNRAS*, 341, 369
- Dolag, K., Bartelmann, M., & Lesch, H. 2002, *A&A*, 387, 383
- Donnert, J., & Brunetti, G. 2014, *MNRAS*, 443, 3564
- Drabent, A., Hoeft, M., Pizzo, R. F., et al. 2015, *A&A*, 575, A8
- Duchesne, S. W., Johnston-Hollitt, M., Offringa, A. R., et al. 2017, *ArXiv e-prints*, arXiv:1707.03517
- Duffy, A. R., Schaye, J., Kay, S. T., & Dalla Vecchia, C. 2008, *MNRAS*, 390, L64
- Eilek, J. A., & Hughes, P. A. 1991, Particle acceleration and magnetic field evolution, ed. P. A. Hughes (Cambridge University Press), 428
- Ettori, S., Donnarumma, A., Pointecouteau, E., et al. 2013, *SSRv*, 177, 119
- Ewall-Wice, A., Dillon, J. S., Liu, A., & Hewitt, J. 2017, *MNRAS*, 470, 1849
- Fan, X., Carilli, C. L., & Keating, B. 2006, *ARA&A*, 44, 415
- Farnsworth, D., Rudnick, L., Brown, S., & Brunetti, G. 2013, *ApJ*, 779, 189
- Feretti, L., Fusco-Femiano, R., Giovannini, G., & Govoni, F. 2001, *A&A*, 373, 106
- Feretti, L., Giovannini, G., & Böhringer, H. 1997, *NewA*, 2, 501
- Feretti, L., Giovannini, G., Govoni, F., & Murgia, M. 2012, *A&A Rv*, 20, 54
- Feretti, L., Schuecker, P., Böhringer, H., Govoni, F., & Giovannini, G. 2005, *A&A*, 444, 157
- Finkbeiner, D. P. 2003, *ApJS*, 146, 407
- Fujita, Y., Takizawa, M., & Sarazin, C. L. 2003, *ApJ*, 584, 190

- Furlanetto, S. R. 2016, *Understanding the Epoch of Cosmic Reionization: Challenges and Progress*, 423, 247
- Furlanetto, S. R., Oh, S. P., & Briggs, F. H. 2006, *PhR*, 433, 181
- Giacintucci, S., Dallacasa, D., Venturi, T., et al. 2011, *A&A*, 534, A57
- Giacintucci, S., Kale, R., Wik, D. R., Venturi, T., & Markevitch, M. 2013, *ApJ*, 766, 18
- Giacintucci, S., Venturi, T., Brunetti, G., et al. 2009a, *A&A*, 505, 45
- Giacintucci, S., Venturi, T., Cassano, R., Dallacasa, D., & Brunetti, G. 2009b, *ApJL*, 704, L54
- Giardino, G., Banday, A. J., Górski, K. M., et al. 2002, *A&A*, 387, 82
- Giovannini, G., Bonafede, A., Feretti, L., et al. 2009, *A&A*, 507, 1257
- Giovannini, G., & Feretti, L. 2000, *NewA*, 5, 335
- Giovannini, G., Feretti, L., Girardi, M., et al. 2011, *A&A*, 530, L5
- Gleser, L., Nusser, A., & Benson, A. J. 2008, *MNRAS*, 391, 383
- Górski, K. M., Hivon, E., Banday, A. J., et al. 2005, *ApJ*, 622, 759
- Govoni, F., & Feretti, L. 2004, *International Journal of Modern Physics D*, 13, 1549
- Govoni, F., Feretti, L., Giovannini, G., et al. 2001, *A&A*, 376, 803
- Govoni, F., Ferrari, C., Feretti, L., et al. 2012, *A&A*, 545, A74
- Govoni, F., Murgia, M., Feretti, L., et al. 2005, *A&A*, 430, L5
- Govoni, F., Murgia, M., Giovannini, G., Vacca, V., & Bonafede, A. 2011, *A&A*, 529, A69
- Gunn, J. E., & Gott, III, J. R. 1972, *ApJ*, 176, 1
- Hogg, D. W. 1999, *ArXiv Astrophysics e-prints*, astro-ph/9905116
- Intema, H. T., van der Tol, S., Cotton, W. D., et al. 2009, *A&A*, 501, 1185
- Jelić, V., Zaroubi, S., Labropoulos, P., et al. 2008, *MNRAS*, 389, 1319
- Jones, C., & Forman, W. 1984, *ApJ*, 276, 38
- Keshet, U., Waxman, E., & Loeb, A. 2004, *NewAR*, 48, 1119
- Kim, K.-T., Kronberg, P. P., Dewdney, P. E., & Landecker, T. L. 1990, *ApJ*, 355, 29
- Kitayama, T., & Suto, Y. 1996, *ApJ*, 469, 480
- Knowles, K., Intema, H. T., Baker, A. J., et al. 2016, *MNRAS*, 459, 4240
- Koopmans, L., Pritchard, J., Mellemma, G., et al. 2015, *Advancing Astrophysics with the Square Kilometre Array (AASKA14)*, 1
- Lacey, C., & Cole, S. 1993, *MNRAS*, 262, 627
- Large, M. I., Mathewson, D. S., & Haslam, C. G. T. 1959, *Nature*, 183, 1663
- Liang, H., Hunstead, R. W., Birkinshaw, M., & Andreani, P. 2000, *ApJ*, 544, 686
- Lindner, R. R., Baker, A. J., Hughes, J. P., et al. 2014, *ApJ*, 786, 49
- Liu, A., Parsons, A. R., & Trott, C. M. 2014, *PhRvD*, 90, 023018
- Liu, A., & Tegmark, M. 2012, *MNRAS*, 419, 3491
- Liu, A., Tegmark, M., & Zaldarriaga, M. 2009, *MNRAS*, 394, 1575
- Macario, G., Venturi, T., Intema, H. T., et al. 2013, *A&A*, 551, A141
- Macario, G., Intema, H. T., Ferrari, C., et al. 2014, *A&A*, 565, A13
- Martinez Aviles, G., Ferrari, C., Johnston-Hollitt, M., et al. 2016, *A&A*, 595, A116
- Mellemma, G., Koopmans, L. V. E., Abdalla, F. A., et al. 2013, *Experimental Astronomy*, 36, 235
- Mesinger, A., Greig, B., & Sobacchi, E. 2016, *MNRAS*, 459, 2342
- Miniati, F. 2015, *ApJ*, 800, 60
- Miniati, F., & Beresnyak, A. 2015, *Nature*, 523, 59
- Mitchell, D. A., Greenhill, L. J., Wayth, R. B., et al. 2008, *IEEE Journal of Selected Topics in Signal Processing*, 2, 707
- Morales, M. F., Bowman, J. D., Cappallo, R., Hewitt, J. N., & Lonsdale, C. J. 2006, *NewAR*, 50, 173
- Morales, M. F., Hazelton, B., Sullivan, I., & Beardsley, A. 2012, *ApJ*, 752, 137
- Morales, M. F., & Hewitt, J. 2004, *ApJ*, 615, 7
- Morales, M. F., & Wyithe, J. S. B. 2010, *ARA&A*, 48, 127
- Mort, B., Dulwich, F., Razavi-Ghods, N., de Lera Acedo, E., & Grainge, K. 2017, *MNRAS*, 465, 3680
- Mort, B. J., Dulwich, F., Salvini, S., Adami, K. Z., & Jones, M. E. 2010, in 2010 IEEE International Symposium on Phased Array Systems and Technology, 690–694
- Murgia, M., Govoni, F., Feretti, L., & Giovannini, G. 2010, *A&A*, 509, A86
- Murgia, M., Govoni, F., Markevitch, M., et al. 2009, *A&A*, 499, 679
- Murray, S. G., Power, C., & Robotham, A. S. G. 2013, *Astronomy and Computing*, 3, 23
- Murray, S. G., Trott, C. M., & Jordan, C. H. 2017, *ApJ*, 845, 7

- Navarro, J. F., Frenk, C. S., & White, S. D. M. 1997, *ApJ*, **490**, 493
- Offringa, A. R., & Smirnov, O. 2017, *MNRAS*, **471**, 301
- Offringa, A. R., McKinley, B., Hurley-Walker, N., et al. 2014, *MNRAS*, **444**, 606
- Pandey-Pommier, M., van Weeren, R. J., Oglean, G. A., et al. 2015, in SF2A-2015: Proceedings of the Annual meeting of the French Society of Astronomy and Astrophysics, ed. F. Martins, S. Boissier, V. Buat, L. Cambrésy, & P. Petit, 247–252
- Park, B. T., & Petrosian, V. 1996, *ApJS*, **103**, 255
- Parsons, A. R., Backer, D. C., Foster, G. S., et al. 2010, *AJ*, **139**, 1468
- Peebles, P. J. E. 1980, The Large-scale Structure of the Universe (Princeton University Press)
- Petrosian, V. 2001, *ApJ*, **557**, 560
- Pindor, B., Wyithe, J. S. B., Mitchell, D. A., et al. 2011, *PASA*, **28**, 46
- Pinzke, A., Oh, S. P., & Pfrommer, C. 2017, *MNRAS*, **465**, 4800
- Press, W. H., & Schechter, P. 1974, *ApJ*, **187**, 425
- Randall, S. W., Sarazin, C. L., & Ricker, P. M. 2002, *ApJ*, **577**, 579
- Reid, A. D., Hunstead, R. W., Lemonon, L., & Pierre, M. M. 1999, *MNRAS*, **302**, 571
- Remazeilles, M., Dickinson, C., Banday, A. J., Bigot-Sazy, M.-A., & Ghosh, T. 2015, *MNRAS*, **451**, 4311
- Rybicki, G. B., & Lightman, A. P. 1979, Radiative Processes in Astrophysics, A Wiley-Interscience publication (Wiley)
- Ryu, D., Kang, H., Cho, J., & Das, S. 2008, *Science*, **320**, 909
- Sanderson, A. J. R., & Ponman, T. J. 2003, *MNRAS*, **345**, 1241
- Sarazin, C. L. 1999, *ApJ*, **520**, 529
- Sarazin, C. L. 2002, in Astrophysics and Space Science Library, Vol. 272, Merging Processes in Galaxy Clusters, ed. L. Feretti, I. M. Gioia, & G. Giovannini, 1–38
- Schlickeiser, R. 2002, Cosmic Ray Astrophysics (Springer)
- Shakouri, S., Johnston-Hollitt, M., & Pratt, G. W. 2016, *MNRAS*, **459**, 2525
- Shaver, P. A., Windhorst, R. A., Madau, P., & de Bruyn, A. G. 1999, *A&A*, **345**, 380
- Smirnov, O. M. 2011, *A&A*, **527**, A106
- Smirnov, O. M., Frank, B. S., Theron, I. P., & Wood, I. H. 2012, in 2012 International Conference on Electromagnetics in Advanced Applications, 586–590
- Spinelli, M., Bernardi, G., & Santos, M. G. 2018, *MNRAS*, **479**, 275
- Thyagarajan, N., Udaya Shankar, N., Subrahmanyam, R., et al. 2013, *ApJ*, **776**, 6
- Tingay, S. J., Goeke, R., Bowman, J. D., et al. 2013, *PASA*, **30**, e007
- Tormen, G., Moscardini, L., & Yoshida, N. 2004, *MNRAS*, **350**, 1397
- Trott, C. M., & Tingay, S. J. 2015, *ApJ*, **814**, 27
- Vacca, V., Govoni, F., Murgia, M., et al. 2011, *A&A*, **535**, A82
- van Haarlem, M. P., Wise, M. W., Gunst, A. W., et al. 2013, *A&A*, **556**, A2
- van Weeren, R. J., Bonafede, A., Ebeling, H., et al. 2012, *MNRAS*, **425**, L36
- van Weeren, R. J., Brüggen, M., Röttgering, H. J. A., et al. 2011, *A&A*, **533**, A35
- van Weeren, R. J., Röttgering, H. J. A., Brüggen, M., & Cohen, A. 2009, *A&A*, **505**, 991
- van Weeren, R. J., Fogarty, K., Jones, C., et al. 2013, *ApJ*, **769**, 101
- van Weeren, R. J., Intema, H. T., Lal, D. V., et al. 2014, *ApJL*, **781**, L32
- Vazza, F., Brunetti, G., Gheller, C., Brunino, R., & Brüggen, M. 2011, *A&A*, **529**, A17
- Vazza, F., Ferrari, C., Bonafede, A., et al. 2015, Advancing Astrophysics with the Square Kilometre Array (AASKA14), 97
- Vazza, F., Roediger, E., & Brüggen, M. 2012, *A&A*, **544**, A103
- Venturi, T., Bardelli, S., Dallacasa, D., et al. 2003, *A&A*, **402**, 913
- Venturi, T., Rossetti, M., Brunetti, G., et al. 2017, *A&A*, **603**, A125
- Wang, J., Xu, H., Gu, J., et al. 2010, *ApJ*, **723**, 620
- Wang, J., Xu, H., An, T., et al. 2013, *ApJ*, **763**, 90
- Wilber, A., Brüggen, M., Bonafede, A., et al. 2018, *MNRAS*, **473**, 3536
- Wilman, R. J., Miller, L., Jarvis, M. J., et al. 2008, *MNRAS*, **388**, 1335
- Wyithe, J. S. B., & Loeb, A. 2004, *Nature*, **432**, 194
- Zaroubi, S. 2013, in Astrophysics and Space Science Library, Vol. 396, The First Galaxies, ed. T. Wiklind, B. Mobasher, & V. Bromm, 45
- Zheng, Q., Wu, X.-P., Johnston-Hollitt, M., Gu, J.-h., & Xu, H. 2016, *ApJ*, **832**, 190